

Pacific-North American teleconnection and North Pacific Oscillation: historical simulation and future projection in CMIP5 models

Zheng Chen¹ · Bolan Gan¹  · Lixin Wu¹ · Fan Jia²

Received: 3 January 2017 / Accepted: 24 August 2017 / Published online: 13 September 2017
© The Author(s) 2017. This article is an open access publication

Abstract Based on reanalysis datasets and as many as 35 CMIP5 models, this study evaluates the capability of climate models to simulate the spatiotemporal features of Pacific-North American teleconnection (PNA) and North Pacific Oscillation (NPO) in the twentieth century wintertime, and further investigates their responses to greenhouse warming in the twenty-first century. Analysis reveals that while the majority (80%) of models reasonably simulate either the geographical distribution or the amplitude of PNA/NPO pattern, only half of models can well capture both features in space. As for the temporal features, variabilities of PNA and NPO in most models are biased toward higher amplitude. Additionally, most models simulate the interannual variabilities of PNA and NPO, qualitatively consistent with the observation, whereas models generally lack the capability to reproduce the decadal (20–25 years) variability of PNA. As the climate warms under the strongest future warming scenario, the PNA intensity is found to be strengthened, whereas there is no consensus on the direction of change in the NPO intensity among models. The intensification of positive PNA is primarily manifested in the large deepening of the North Pacific trough, which is robust as it is 2.3 times the unforced internal variability. By focusing on the tropical Pacific Ocean, we find that the multidecadal evolution of the North Pacific trough intensity (dominating the PNA

intensity evolution) is closely related to that of the analogous trough in the PNA-like teleconnection forced by sea surface temperature anomalies (SSTa) in the tropical central Pacific (CP) rather than the tropical eastern Pacific (EP). Such association is also found to act under greenhouse warming: that is, the strengthening of the PNA-like teleconnection induced by the CP SSTa rather than the EP SSTa is a driving force for the intensification of PNA. This is in part owing to the robust enhancement of the tropical precipitation response to the CP SST variation. Indeed, further inspection suggests that models with stronger intensification of the CP SST variability and its related tropical precipitation response tend to have larger deepening magnitude of the North Pacific trough associated with the PNA variability.

Keywords Global warming · Pacific-North American teleconnection · North Pacific Oscillation · Tropical Pacific Ocean · CMIP5 climate models

1 Introduction

As two important members of the teleconnection family in the Northern Hemisphere, the Pacific-North American teleconnection (PNA) and North Pacific Oscillation (NPO), are prominent modes of planetary-scale atmospheric variability over the North Pacific basin, with additional centers of action across the North American landmass for the PNA. The PNA is identified as geopotential height (GPH) fluctuations, whose positive phase is featured by four centers, such that two centers with above-normal heights are located near Hawaii (20°N, 160°W) and over Alberta, Canada (55°N, 115°W), and the other two with below-normal heights are centered over the North Pacific Ocean (45°N, 165°W) and over the Gulf Coast region of the United States (30°N,

✉ Bolan Gan
gbl0203@ouc.edu.cn

¹ Physical Oceanography Laboratory, Ocean University of China and Qingdao National Laboratory for Marine Science and Technology, 5 Yushan Road, Qingdao 266003, People's Republic of China

² Key Laboratory of Ocean Circulation and Waves, Institute of Oceanology, Chinese Academy of Sciences, Qingdao, People's Republic of China

85°W) (Wallace and Gutzler 1981). The NPO is characterized as a meridional dipole of the sea level pressure (SLP), with the positive phase featured by a zonally elongated band of above-normal SLP in the subtropics and a center of below-normal SLP over Alaska. Linkin and Nigam (2008) further pointed out that the NPO is the SLP signature of the West Pacific (WP) teleconnection pattern in the upper-level geopotential height, which is the second leading mode behind the PNA mode (Wallace and Gutzler 1981).

Both the PNA and NPO, prominent in boreal winter, have close relationships with fluctuations in the position and strength of the Asian-Pacific jet stream and the North Pacific storm tracks, and have powerful influences on the North American hydroclimate. The positive PNA is associated with the enhancement and eastward extension of the jet stream, while the northward displacement and elongation of the jet exit region is linked to the positive NPO, and vice versa (e.g., Linkin and Nigam 2008; Wettstein and Wallace 2010). Under the framework of eddy-mean flow interaction, the PNA and NPO also modulate variations of storm tracks in association with the anomalous jet, such as a southward shift and downstream intensification of storm tracks corresponding to the positive phases of the PNA and NPO, respectively (Lau 1988; Rogers 1990; Wettstein and Wallace 2010). These dynamical changes are expected to impact the surface climate of North America especially in winter (e.g., Leathers et al. 1991; Nigam 2003). Particularly, previous studies demonstrated intimate connections of the PNA with the atmospheric blocking frequency in the North Pacific (Crocini-Maspoli et al. 2007), the North American snow depth (Ge and Gong 2009), as well as the heavy rainfall events in the north central United States (Harding and Snyder 2015). The NPO also is very influential on the winter surface air temperature and precipitation over much of the western North America as well as the marginal ice zone in the western Bering Sea and Sea of Okhotsk (Linkin and Nigam 2008).

Furthermore, the PNA's signature on the Aleutian Low is closely related to the Pacific Decadal Oscillation (PDO; e.g., Latif and Barnett 1996; Deser et al. 2004), the dominant pattern of the decadal climate variability in the North Pacific, while the NPO is demonstrated as the atmospheric forcing pattern of the North Pacific Gyre Oscillation (NPGO; e.g., Di Lorenzo et al. 2008; Chhak et al. 2009), the second leading mode of the North Pacific Ocean. In addition, both the PNA and NPO play an active role in connecting climate variabilities in the tropical and extratropical Pacific. On one hand, the El Niño-Southern Oscillation (ENSO) variability influences the surface climate over the North Pacific Rim through inducing the atmospheric PNA-like changes (Alexander et al. 2002), and the central Pacific El Niño events in winter can excite the low-frequency variations of the southern lobe of NPO

which is integrated to yield the oceanic NPGO (Di Lorenzo et al. 2010). On the other hand, the NPO change during the decay phase of traditional type of ENSO can help lead to the onset of central Pacific type of ENSO (Yu and Kim 2011).

Given that the PNA and NPO remarkably affect the North Pacific and North American hydroclimate, and thus their long-term shifts in space-time could change the preconditions that determine the surface climate, it is worthwhile to comprehensively evaluate the capability of coupled climate models to reproduce both modes in the past climate, and to explore how they may change in the future under greenhouse warming. However, such issues have not yet been fully addressed. For instance, Stoner et al. (2009) assessed the performance of Coupled Model Intercomparison Project Phase 3 (CMIP3) climate models to simulate the PNA, primarily focusing on its spatial characteristics, and found that the majority of models capture a recognizable winter PNA pattern but overestimate the percentage of total variance in heights explained by the PNA variability. They did not examine the frequency and amplitude of the modeled PNA and its change in the future projection. Allan et al. (2014), however, reported more positive PNA events would occur in future and consequently have a stronger influence on North American climate, based on the Special Report on Emissions Scenarios (SRES) A2 projection in a global coupled model. Using the CMIP3 multi-model outputs of the twentieth century and A1B scenario experiments, Furtado et al. (2011) found that the NPO pattern linked to the NPGO-like sea surface temperature (SST) anomalies remains unchanged spatially under greenhouse warming. Overall, the latest Fifth Assessment Report of Intergovernmental Panel on Climate Change (IPCC AR5) summarized that an issue of the model-projected future evolution of the PNA and NPO remains to be fully addressed (Christensen et al. 2013). It motivates us to deal with the following two questions: (1) how well does the current generation of global climate models participating in the CMIP5 (CMIP Phase 5) portray the observed spatiotemporal features of PNA/NPO in the twentieth century? (2) Will the PNA/NPO significantly change in the future warming projection? If changed, what mechanism could be involved?

The paper is organized as follows. Section 2 describes the observational datasets, multi-model outputs and analysis methods. Section 3 compares the spatiotemporal features of PNA and NPO in the twentieth century between observations and historical simulations of CMIP5 models. Section 4 shows the twenty-first century projected changes in the PNA and NPO under the Representative Concentration Pathways 8.5 (RCP8.5) scenario. In Sect. 5, we investigate the possible mechanism driving the significant response of PNA to greenhouse warming with focus on the influence of tropical Pacific Ocean. Summary and discussion is given in Sect. 6.

2 Datasets and methods

2.1 Observations and multi-model outputs

The PNA and NPO in observation are investigated based on GPH and SLP data taken from the ensemble-mean fields of Twentieth-Century Reanalysis dataset version 2c (20CRv2c), with a horizontal resolution of $2^\circ \times 2^\circ$ and 24 vertical pressure levels (Compo et al. 2011). Note that we also examine the newly-developed European Centre for Medium-Range

Weather Forecasts (ECMWF) twentieth Century Reanalysis (ERA-20C; Poli et al. 2016) and obtain similar results, as the spatiotemporal features of PNA/NPO derived from both datasets are highly correlated (not shown). To investigate oceanic influences, we also use SST data taken from the Met Office Hadley Centre Sea Ice and Sea Surface Temperature version 1 (HadISST1) dataset, with a horizontal resolution of $1^\circ \times 1^\circ$ (Rayner et al. 2003).

For model simulations, we investigate 35 CMIP5 models in total (Table 1), organized by the Program for Climate

Table 1 List of 35 CMIP5 models analyzed in the present study

| Institution, Country | Model name | Spatial resolution of AGCM (lon \times lat) |
|---|----------------|---|
| Commonwealth Scientific and Industrial Research Organisation and Bureau of Meteorology, Australia | ACCESS1.0 | $1.875^\circ \times 1.25^\circ$ |
| | ACCESS1.3 | $1.875^\circ \times 1.25^\circ$ |
| Beijing Climate Center, China Meteorological Administration, China GCESS, BNU, China | BCC-CSM1.1 | $2.8^\circ \times 2.8^\circ$ |
| | BNU-ESM | $2.8^\circ \times 2.8^\circ$ |
| Canadian Centre for Climate Modelling and Analysis, Canada National Center for Atmospheric Research Boulder, USA | CanESM2 | $2.8^\circ \times 2.8^\circ$ |
| | CCSM4 | $1.25^\circ \times 0.9^\circ$ |
| NSF/DOE National Center for Atmospheric Research Boulder, USA | CESM1(BGC) | $1.25^\circ \times 0.9^\circ$ |
| | CESM1(CAM5) | $1.25^\circ \times 0.9^\circ$ |
| Centro Euro-Mediterraneo per i Cambiamenti Climatici, Italy | CMCC-CESM | $3.75^\circ \times 3.75^\circ$ |
| | CMCC-CM | $0.75^\circ \times 0.75^\circ$ |
| Centre National de Recherches Meteorologiques, Meteo-France, and Centre Europeen de Recherches et de Formation Avancee en Calcul Scientifique, France | CNRM-CM5 | $1.4^\circ \times 1.4^\circ$ |
| | CSIRO-Mk3.6.0 | $1.875^\circ \times 1.875^\circ$ |
| Australian Commonwealth Scientific and Industrial Research Organization Marine and Atmospheric Research in collaboration with the Queensland Climate Change Centre of Excellence, Australia | EC-EARTH | $1.125^\circ \times 1.125^\circ$ |
| | FGOALS-g2 | $2.8^\circ \times 2.8^\circ$ |
| Institute of Atmospheric Physics, Chinese Academy of Sciences, Tsinghua University, China The First Institution of Oceanography, China | FIO-ESM | $2.8^\circ \times 2.8^\circ$ |
| | GFDL-CM3 | $1.25^\circ \times 2^\circ$ |
| NOAA Geophysical Fluid Dynamics Laboratory, USA | GFDL-ESM2G | $1.25^\circ \times 2^\circ$ |
| | GISS-E2-H | $2.5^\circ \times 2^\circ$ |
| NASA Goddard Institute for Space Studies, USA | GISS-E2-R | $2.5^\circ \times 2^\circ$ |
| | HadGEM2-AO | $1.875^\circ \times 1.25^\circ$ |
| National Institute of Meteorological Research, South Korea | HadGEM2-CC | $1.875^\circ \times 1.25^\circ$ |
| | HadGEM2-ES | $1.875^\circ \times 1.25^\circ$ |
| Institute for Numerical Mathematics, Russia Institut Pierre Simon Laplace, France | INM-CM4 | $2^\circ \times 1.5^\circ$ |
| | IPSL-CM5A-LR | $3.75^\circ \times 1.875^\circ$ |
| Japan Agency for Marine-Earth Science and Technology, Atmosphere and Ocean Research Institute, The University of Tokyo, and National Institute for Environmental Studies, Japan | IPSL-CM5A-MR | $2.5^\circ \times 1.25^\circ$ |
| | IPSL-CM5B-LR | $3.75^\circ \times 1.875^\circ$ |
| Max Planck Institute for Meteorology, Germany | MIROC-ESM | $2.8^\circ \times 2.8^\circ$ |
| | MIROC-ESM-CHEM | $2.8^\circ \times 2.8^\circ$ |
| Meteorological Research Institute, Japan | MIROC5 | $1.4^\circ \times 1.4^\circ$ |
| | MPI-ESM-LR | $1.875^\circ \times 1.875^\circ$ |
| Norwegian Climate Centre, Norway | MPI-ESM-MR | $1.875^\circ \times 1.875^\circ$ |
| | MRI-CGCM3 | $1.125^\circ \times 1.125^\circ$ |
| | MRI-ESM1 | $1.125^\circ \times 1.125^\circ$ |
| | NorESM1-M | $2.5^\circ \times 1.875^\circ$ |
| | NorESM1-ME | $2.5^\circ \times 1.875^\circ$ |

Model Diagnosis and Intercomparison for IPCC AR5 (Taylor et al. 2012). Multi-model outputs from three sets of simulations are used: the pre-industrial control (PI) simulation which represents the unforced natural variability of climate system with atmospheric CO₂ concentration fixed at 280–290 ppm; the historical simulation which incorporates the anthropogenic and natural forcings from the observed atmospheric composition changes in the twentieth century; the future climate change projection under the RCP8.5 scenario in the twenty-first century, with the radiation forcing reaching approximately 8.5Wm⁻² in 2100 (equivalent to atmospheric CO₂ concentration >1370 ppm). In Sect. 3, we use GPH (SLP) outputs of 30 (32) models from the historical simulation to evaluate the capability of simulating the spatiotemporal features of PNA (NPO) in the twentieth century. Then, models which relatively well simulate both the geographical distribution and the amplitude of PNA/NPO pattern are selected to further investigate the future projected response of PNA/NPO to greenhouse warming by means of comparing statistics between the historical and RCP8.5 runs. In Sects. 4 and 5, we use additional outputs of the selected models, including SST and precipitation. The atmospheric fields are interpolated to 2.5° × 2.5° grid, except for precipitation, which is interpolated to 1° × 1° grid, and so does the SST field. Here, we choose 95-year interval in the twentieth century (1900–1994) and twenty-first century (2006–2100) to represent the past and future climate, respectively. In fact, the spatial pattern of PNA/NPO is generally insensitive to temporal-interval selection (such as 95- versus 45-year in the second half of the century), which thus does not greatly affect our conclusions. Only one member (“r1i1p1”) run for each model is used in the present study.

2.2 PNA/NPO pattern and its intensity

Previous studies define the PNA index in different ways. Wallace and Gutzler (1981) first defined it as a linear combination of four centers of normalized 500-hPa GPH anomalies (GPHa). Based on rotated principal component analysis (RPCA) or PCA method, other literatures also used the first leading principle component (PC1) of 500-hPa GPHa as the PNA index (Barnston and Livezey 1987; Stoner et al. 2009). Given that, we first obtain the regression pattern of monthly detrended 500-hPa GPHa against the PNA index provided by the Climate Prediction Center (CPC), and then compare such pattern with the regression pattern developed by regressing the 500-hPa GPHa onto the PC1 time series which are derived by applying empirical orthogonal function (EOF) or rotated EOF (REOF, i.e. varimax rotation) to the 500-hPa GPHa field. Two domains, i.e., the Northern Hemisphere (poleward of 10°N) and the North Pacific (10°–80°N, 150°E–60°W) are analyzed and the temporal coverage is 1950–1994. We

calculate the spatial correlation between the CPC regression pattern and the EOF/REOF pattern in each domain. Results show that the North Pacific EOF pattern highly resembles the CPC regression pattern, with correlation coefficient $r_{EOF} = 0.83$ versus $r_{REOF} = 0.58$, whereas correlations for the Northern Hemisphere domain are much lower, with $r_{EOF} = 0.55$ and $r_{REOF} = 0.44$. Therefore, the EOF-based method using 500-hPa GPHa field in the North Pacific is chosen to construct the PNA index for both observation and models. The NPO index is defined as the second leading PC (PC2) of SLP anomalies (SLPa) in the region bounded by 10°–80°N and 120°E–60°W (Linkin and Nigam 2008).

In the present study, monthly December–January–February (DJF) anomalies are used for the EOF and regression analyses, as both the PNA and NPO are prominent in boreal winter. Monthly anomalies are first obtained by subtracting the climatological monthly means and removing the linear trend, and then they are smoothed by 3-month running mean to extract the DJF anomalies. Prior to EOF analysis, GPHa and SLPa fields are weighted by the square root of the cosine of latitude to account for the decrease of grid area poleward. The PNA/NPO pattern is derived by regressing the monthly DJF anomalous field onto the normalized PNA/NPO index (i.e., the PC1 of 500-hPa GPHa for PNA; the PC2 of SLPa for NPO), which represents the typical amplitude of PNA/NPO (i.e., one standard deviation of index). Note that the PNA/NPO pattern is calculated for the historical run and the RCP8.5 run separately, and their difference in amplitude indicates the response to greenhouse warming.

Based on the geographical distribution of PNA/NPO, we define the PNA intensity (PNA_i) and the NPO intensity (NPO_i) as a linear combination of centers of action:

$$PNA_i = PNAa_i + (-PNAb_i) + PNAc_i + (-PNAd_i)$$

$$NPO_i = (-NPOa_i) + NPOb_i$$

where $PNAa_i$, $-PNAb_i$, $PNAc_i$, $-PNAd_i$ denote the intensities of four centers of PNA quadrupole in positive phase as shown in Fig. 3a, and likewise $-NPOa_i$ and $NPOb_i$ stand for the intensities of two centers of NPO dipole in positive phase as shown in Fig. 3c. The intensity of each center of PNA (NPO) is computed as the five-points-mean of central GPHa (SLPa), i.e., central maxima or minima plus four orthogonal values around the center. In the present study, the sign of PNA/NPO pattern for both the observation and individual model simulations is kept in its positive phase, so that the value of each center intensity (e.g., $-PNAb_i$) is positive.

It is noted that the multi-model ensemble mean (MEM) statistics are calculated as the mean of the individual statistic being analyzed. For example, the MEM pattern of PNA is computed as the mean of individual patterns in positive phase which are derived by the regression of 500-hPa GPHa

field in DJF onto the normalized PNA index from individual models.

2.3 Spectral analysis

To investigate the temporal variability of PNA/NPO, we apply the spectral analysis on the monthly expansion coefficient (EC) time series, instead of the wintertime PNA/NPO index, since the latter is a filtered and inconsecutive time series (see Sect. 2.2 for details). Following Furtado et al. (2011), the monthly EC time series is constructed by projecting the unfiltered monthly GPHa/SLPa fields onto the wintertime PNA/NPO pattern, which thus mainly preserves the prominent features of PNA/NPO. Here all power spectra are normalized so that the percentage of total variance explained at a particular frequency is presented in the power spectra. The significance test of power spectra is based on the method proposed by Torrence and Compo (1998). The mean normalized red-noise spectrum is calculated for the monthly EC time series of PNA/NPO and then the 90% confidence spectrum is obtained by multiplying the red-noise spectrum by the appropriate F statistic. Only peaks of power spectra exceeding the 90% confidence spectrum as a function of period are plotted.

2.4 Estimation of unforced internal variability in CMIP5 models

To test the significance of projected changes in the PNA and NPO variability forced by greenhouse warming, we calculate the unforced internal variability of both modes based on the PI run for each model. First, we construct 41 segments with time increment of 95-year, for which the starting year of each one was taken 10-year apart from the 500-year long (after spin-up) outputs of the PI run. These 41 segments are considered independent of each other under the assumption that atmospheric states among different segments are uncorrelated. Then, total 41 PNA/NPO patterns in positive phase, corresponding to one standard deviation of PNA/NPO index, are derived from 41 segments. Indeed, further inspection finds no significant correlations of PNA/NPO index between consecutive two segments. Finally, we calculate the intensity of each PNA/NPO pattern, and the standard deviation of intensities across 41 patterns is used to measure the unforced internal variability of PNA/NPO.

3 PNA and NPO in the past: observation versus model simulation

First, we evaluate the capability of CMIP5 models to portray the spatial features of PNA and NPO in the twentieth century (1900–1994), by employing Taylor diagrams (Taylor 2001),

which are particularly useful in assessing the relative merits of models. Here 30 and 32 models are assessed for the PNA and NPO, respectively, depending on the availability of data archive. Taylor diagrams are constructed based on three statistics, i.e., the spatial correlation coefficient between the simulated and observed patterns, the standard deviation of PNA/NPO pattern, and the centered pattern root-mean-square difference (CRMS) within the target regions [i.e., PNA (10°–80°N, 150°E–60°W) and NPO (10°–80°N, 120°E–60°W)]. The CRMS of each simulation (\mathbf{m}) with respect to observation (\mathbf{f}) is defined as:

$$\text{CRMS} = \left\{ \frac{1}{N} \sum_{n=1}^N [(f_n - \bar{f}) - (m_n - \bar{m})]^2 \right\}^{1/2}$$

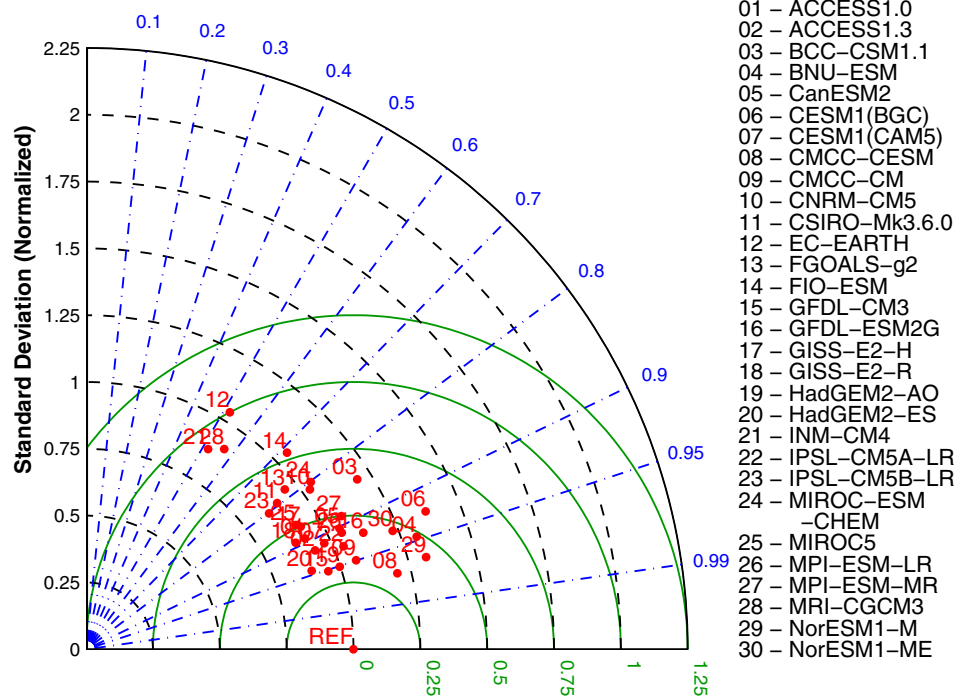
where \bar{f} and \bar{m} are the mean values, and N is the number of grid points. CRMS gives comprehensive information on whether two patterns have similar structure and amplitude of variation. Therefore, in Fig. 1, the smaller the normalized CRMS [i.e., the distance between a model and the observation (referred to as REF)] is, the better performance of the model is.

As shown in Fig. 1, 80% of the models display spatial correlations higher than 0.80 for both PNA and NPO, and 85% (75%) of the models display the normalized standard deviation within the range of $1 \pm 20\%$ for the PNA (NPO) pattern. This suggests that the majority of models reasonably simulate either the geographical distribution or the amplitude of PNA/NPO pattern. However, spatial correlations vary largely among models, especially for NPO, such that it ranges from 0.52 (INM-CM4) to 0.97 (CMCC-CESM) for the PNA and from 0.29 (MIROC-ESM) to 0.97 (IPSL-CM5A-LR) for the NPO. Owing to this large inter-model spread, a similar situation exists with the normalized CRMS. It ranges from 0.31 (GFDL-CM3) to 0.99 (EC-EARTH) for the PNA, with values of 17 models lower than 0.5, and for NPO it ranges from 0.28 (ACCESS1.0) to 1.21 (MIROC-ESM), with values of 16 models lower than 0.5. Therefore, in general, half of models can reliably reproduce both the spatial structure and amplitude of PNA and NPO pattern. Compared with the PNA simulations, however, the ability to simulate the NPO is worse and more dispersed among models.

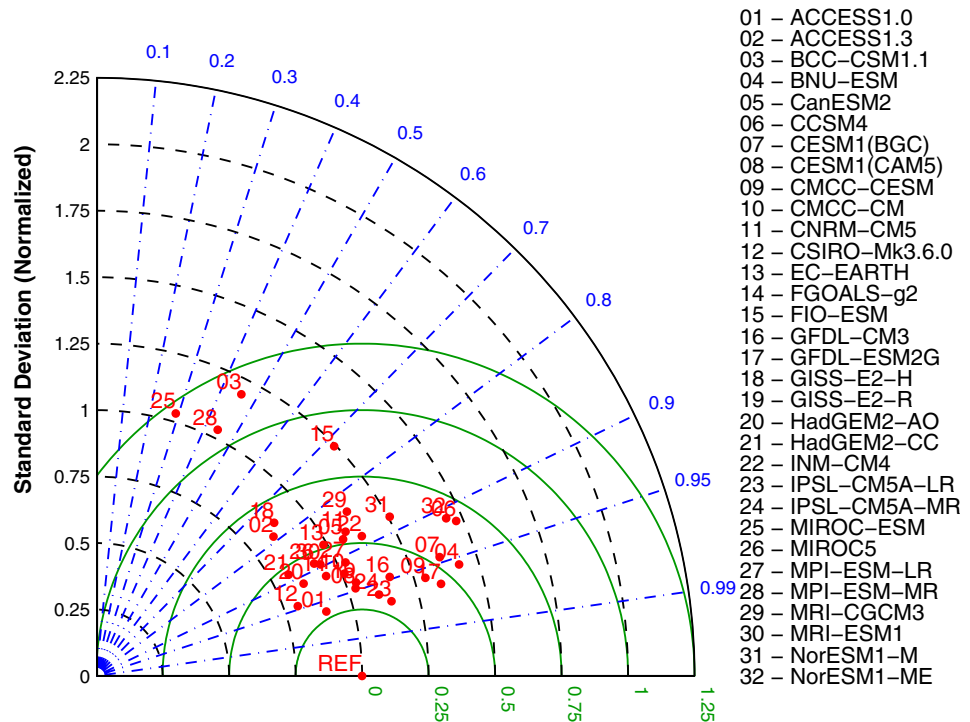
Next, we compare the temporal features of the PNA/NPO between models and observation in the twentieth century, specifically the variance of the monthly EC time series (Table 2) and the percentage of total variance in 500-hPa-GPH (SLP) explained by the PNA (NPO) variability (Table 3). Table 2 suggests that most models have larger variances than the observation for both PNA and NPO, with 18 (22) out of 30 (32) models having variances that are at least 10% higher than the observed variance of

Fig. 1 Taylor diagrams for displaying normalized pattern statistics of **a** PNA and **b** NPO in winter for the reference period 1900–1994. Standard deviation and the centered pattern RMS difference are normalized by the observational standard deviation. Normalized standard deviation and spatial correlation coefficient of a model are given by the radial distance from the origin (*black dashed line*) and the azimuthal position of the model (*blue dot-dashed line*), respectively. The distance from the REF (i.e., observation) to a red point (i.e., a model) is the normalized CRMS (*green solid line*)

(a) Taylor Diagram for the PNA in CMIP5 Historical Simulation



(b) Taylor Diagram for the NPO in CMIP5 Historical Simulation



PNA (NPO). Only 2 (4) models have variance for the PNA (NPO) slightly smaller than the observation. Therefore, the temporal variabilities of PNA and NPO in the majority of models are biased toward higher amplitude. We also find

that no model can simulate the observed phases of PNA and NPO (not shown). Moreover, Table 3 shows that the percentage of total variance in heights explained by the PNA variability is underestimated by most CMIP5 models (21/30),

Table 2 Normalized variance (i.e., actual variance in each model divided by the observational counterpart) of the monthly EC time series for PNA/NPO in CMIP5 historical simulation

| Model name | PNA | NPO |
|----------------|-------|-------|
| ACCESS1.0 | 1.064 | 1.262 |
| ACCESS1.3 | 1.135 | 1.194 |
| BCC-CSM1.1 | 0.997 | 0.923 |
| BNU-ESM | 1.137 | 1.260 |
| CanESM2 | 1.080 | 0.973 |
| CCSM4 | N/A | 1.170 |
| CESM1(BGC) | 0.999 | 1.303 |
| CESM1(CAM5) | 1.016 | 1.274 |
| CMCC-CESM | 1.227 | 1.039 |
| CMCC-CM | 1.180 | 1.286 |
| CNRM-CM5 | 1.225 | 1.000 |
| CSIRO-Mk3.6.0 | 1.009 | 1.269 |
| EC-EARTH | 1.143 | 1.047 |
| FGOALS-g2 | 1.021 | 1.197 |
| FIO-ESM | 1.038 | 0.922 |
| GFDL-CM3 | 1.225 | 1.119 |
| GFDL-ESM2G | 1.124 | 1.022 |
| GISS-E2-H | 1.227 | 1.097 |
| GISS-E2-R | 1.271 | 1.165 |
| HadGEM2-AO | 1.109 | 1.118 |
| HadGEM2-CC | N/A | 1.294 |
| HadGEM2-ES | 1.226 | N/A |
| INM-CM4 | 1.241 | 1.130 |
| IPSL-CM5A-LR | 1.153 | 1.179 |
| IPSL-CM5A-MR | N/A | 1.321 |
| IPSL-CM5B-LR | 1.069 | N/A |
| MIROC-ESM | N/A | 0.933 |
| MIROC-ESM-CHEM | 1.172 | N/A |
| MIROC5 | 1.021 | 1.157 |
| MPI-ESM-LR | 1.231 | 1.224 |
| MPI-ESM-MR | 1.152 | 1.061 |
| MRI-CGCM3 | 1.040 | 1.329 |
| MRI-ESM1 | N/A | 1.415 |
| NorESM1-M | 1.027 | 1.319 |
| NorESM1-ME | 1.200 | 1.188 |
| Observation | 1.000 | 1.000 |

however, which is contrary to the simulations of CMIP3 models (Stoner et al. 2009). As for the NPO variability, 19 out of 32 models show significant biases (>10%) in the percentage of total variance in SLP, in which ten models show bias toward higher percentage and the other nine models show the opposite. It suggests that biases in the percentage of total variance in SLP explained by the NPO variability are either too high or too low.

To further assess the frequency of PNA and NPO variability, we apply the spectral analysis to the monthly EC

time series. For PNA (Fig. 2a), the observed power spectra exhibit multiple spectral peaks within 1 year, which is also shown in individual models albeit at varying frequency. Besides that, the observation displays significant power on interannual time scales, with two peaks in the range of 1–2 and 4–6 years, as well as broad decadal-scale spectrum, with the highest power in the 20–25 years. On interannual time scales, over half of models have significant peaks in the 1–6 years, in which 20 and 15 models exhibit peaks at 1–2 and 4–6 years, with power mostly smaller and larger than the observational counterpart, respectively (Fig. 2c). However, on decadal time scales, only two models have significant peaks at 20–25 years. For NPO (Fig. 2b), the power spectra in both observation and models exhibit multiple peaks within 1 year, while for longer time scale there is only significant peak at 2–4 years in observation. Figure 2d further shows that most models (27/32) have significant peaks in the 1–2 years, whereas 14 models have peaks at 2–4 years, with power mostly larger than the observation. In summary, the majority of models can simulate the interannual variabilities of PNA and NPO, qualitatively consistent with the observation, albeit with the significant spectral peaks varying in the range of 1–6 years. However, models generally lack the ability to reproduce power spectrum of PNA in the decadal band (20–25 years).

As future projections rely on the climate simulation of the twentieth century, vast diversity in the performance of models results in large uncertainty in the projected change. Thus, to better understand the projected changes in PNA and NPO, we select 14 and 13 models which relatively well represent the observed structure and amplitude of PNA and NPO in space, respectively, according to the criterion that the spatial correlation coefficient is larger than 0.9 and the normalized CRMS is lower than 0.5. Here seven models [ACCESS1.3, CESM1(CAM5), CMCC-CESM, CMCC-CM, GFDL-CM3, GFDL-ESM2G, IPSL-CM5A-LR] are selected for both PNA and NPO, and additional seven models (BNU-ESM, CanESM2, HadGEM2-AO, HadGEM2-ES, MPI-ESM-LR, NorESM1-M, NorESM1-ME) and six models (CSIRO-Mk3.6.0, FGOALS-g2, GISS-E2-R, HadGEM2-AO, IPSL-CM5A-MR, MPI-ESM-LR) are retained for the PNA and NPO, respectively.

Figure 3 shows the MEM of PNA/NPO patterns derived from the selected models and the observational counterpart. The MEM patterns of both PNA and NPO well match with the observations, with the spatial correlation coefficient reaching 0.98, and particularly well capture the trough over the North Pacific Ocean (hereinafter referred to as *the* North Pacific trough; denoted as PNAb) and the anomalous low pressure over Alaska (denoted as NPOa). But it is obvious that the MEM pattern of PNA overestimates the ridge over western Canada (denoted as PNAc)

Table 3 Percentage of total variance in 500-hPa-GPH (SLP) explained by the PNA (NPO) pattern in the historical run for all models and the RCP8.5 run for the selected models

| Models for PNA | Historical (%) | RCP8.5 (%) | Δ (%) | Models for NPO | Historical (%) | RCP8.5 (%) | Δ (%) |
|----------------|----------------|------------|--------------|----------------|----------------|------------|--------------|
| ACCESS1.3 | 32.7 | 37.8 | 5.1 | ACCESS1.0 | 18.9 | 19.0 | 0.1 |
| BNU-ESM | 34.6 | 42.0 | 7.4 | CESM1(CAM5) | 17.3 | 17.7 | 0.4 |
| CanESM2 | 32.4 | 41.0 | 8.6 | CMCC-CESM | 21.6 | 17.15 | -4.5 |
| CESM1(CAM5) | 30.2 | 36.8 | 6.6 | CMCC-CM | 18.2 | 19.75 | 1.5 |
| CMCC-CESM | 33.0 | 37.1 | 4.1 | CSIRO-Mk3.6.0 | 14.2 | 18.9 | 4.7 |
| CMCC-CM | 29.0 | 25.8 | -3.2 | FGOALS-g2 | 14.9 | 16.3 | 1.4 |
| GFDL-CM3 | 27.8 | 33.4 | 5.6 | GFDL-CM3 | 19.8 | 20.1 | 0.3 |
| GFDL-ESM2G | 29.1 | 33.4 | 4.3 | GFDL-ESM2G | 24.6 | 24.2 | -0.4 |
| HadGEM2-AO | 29.1 | 35.2 | 6.1 | GISS-E2-R | 22.2 | 19.2 | -3.0 |
| HadGEM2-ES | 25.7 | 32.3 | 6.6 | HadGEM2-AO | 18.0 | 19.0 | 1.0 |
| IPSL-CM5A-LR | 29.3 | 34.7 | 5.4 | IPSL-CM5A-LR | 18.7 | 20.4 | 1.7 |
| MPI-ESM-LR | 25.1 | 33.9 | 8.8 | IPSL-CM5A-MR | 17.0 | 17.6 | 0.6 |
| NorESM1-M | 37.4 | 34.7 | -2.7 | MPI-ESM-LR | 18.9 | 18.6 | -0.3 |
| NorESM1-ME | 31.6 | 36.4 | 4.8 | ACCESS1.3 | 16.3 | N/A | |
| ACCESS1.0 | 26.6 | N/A | | BCC-CSM1.1 | 22.5 | | |
| BCC-CSM1.1 | 29.4 | | | BNU-ESM | 20.9 | | |
| CESM1(BGC) | 37.5 | | | CanESM2 | 22.3 | | |
| CNRM-CM5 | 27.7 | | | CCSM4 | 22.9 | | |
| CSIRO-Mk3.6.0 | 31.9 | | | CESM1(BGC) | 18.6 | | |
| EC-EARTH | 27.4 | | | CNRM-CM5 | 23.3 | | |
| FGOALS-g2 | 28.8 | | | EC-EARTH | 20.6 | | |
| FIO-ESM | 25.8 | | | FIO-ESM | 25.4 | | |
| GISS-E2-H | 25.1 | | | GISS-E2-R | 22.2 | | |
| GISS-E2-R | 24.9 | | | HadGEM2-CC | 17.3 | | |
| INM-CM4 | 27.0 | | | INM-CM4 | 28.0 | | |
| IPSL-CM5B-LR | 22.8 | | | MIROC-ESM | 20.3 | | |
| MIROC-ESM-CHEM | 26.7 | | | MIROC5 | 16.5 | | |
| MIROC5 | 24.8 | | | MPI-ESM-MR | 21.4 | | |
| MPI-ESM-MR | 25.7 | | | MRI-CGCM3 | 15.7 | | |
| MRI-CGCM3 | 26.2 | | | MRI-ESM1 | 13.8 | | |
| | | | | NorESM1-M | 18.5 | | |
| | | | | NorESM1-ME | 23.7 | | |
| Observation | 29.8 | N/A | | Observation | 20.0 | N/A | |

The models that have not been chosen are listed in lower rows (in alphabetical order) and observations are given at the bottom

Δ denotes RCP8.5 minus historical

but underestimates the trough over the Gulf Coast region of the United States (denoted as PNAd), and the MEM pattern of NPO underestimates the anomalous high pressure in the subtropics (denoted as NPOb). Specifically, the simulated magnitude of PNAc (PNAd) center is larger (lower) than the observational counterpart of 42.0 m (-42.3 m) by 26% (30%), and for NPOb the simulated center is lower than the observation of 3.5 hPa by 23%.

4 Future projected changes in the PNA and NPO under greenhouse warming

In this section, we aim at finding out how the PNA and NPO will respond to greenhouse warming in the twenty-first century, with focus on changes in the intensity (see Sect. 2.2 for the definition of PNA/NPO intensity). As aforementioned, we inspect the projected changes in PNA (NPO) in the selected 14 (13) models which relatively well represent the observed spatial features.

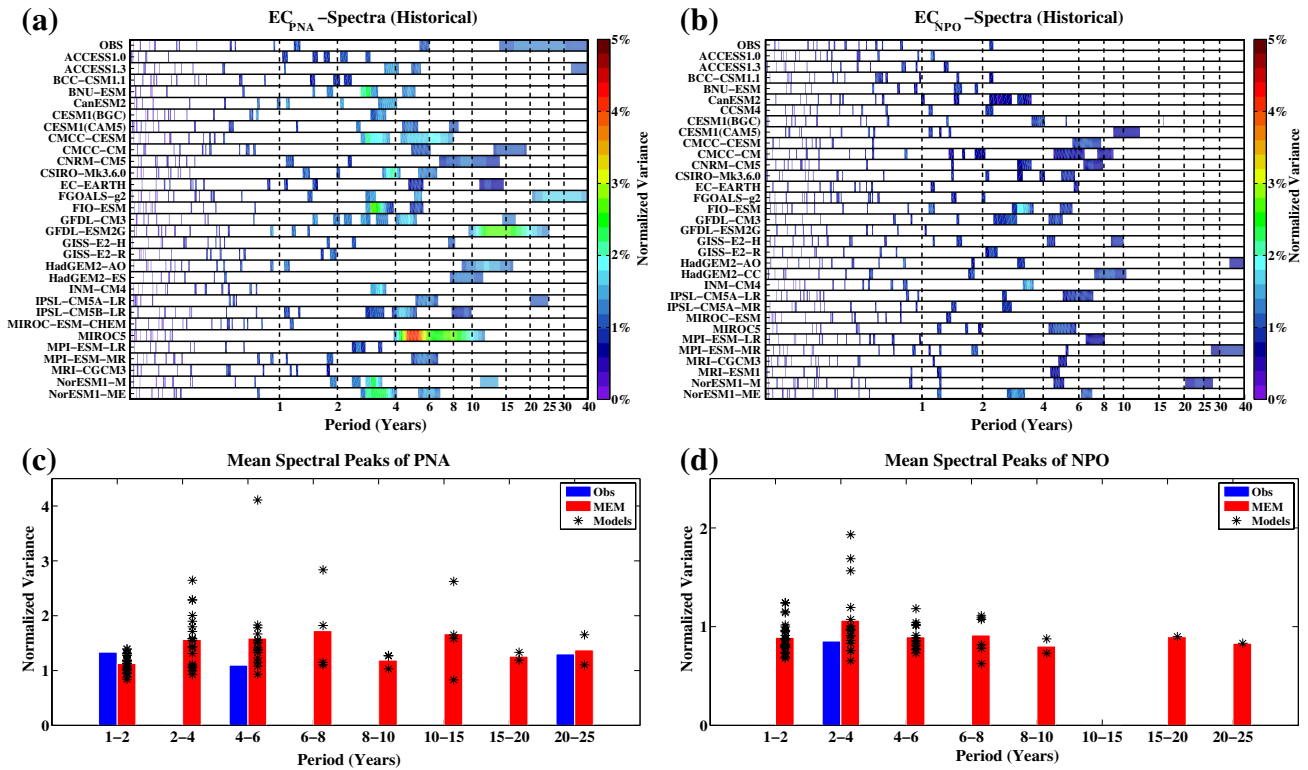


Fig. 2 Power spectra (% of total variance explained) of the monthly EC time series of **a** PNA and **b** NPO for observations and CMIP5 historical simulations. Only significant power values (over the 90% confidence level) are shaded. Histograms of mean spectral peaks of the

monthly EC time series of **c** PNA and **d** NPO, which are derived by averaging the significant spectral peaks in the bins of period in years shown on the x-axis. Normalized variance is shown on the y-axis and asterisk denotes the model which has a peak in the specific bin

4.1 PNA

Figure 4 displays the projected changes in the intensities of PNA/NPO and its each center from the historical run to the RCP8.5 run in the selected models. The projected change is considered significant when the magnitude exceeds the unforced internal variability which is measured based on the PI run. As shown in Fig. 4a, 13 out of 14 models exhibit significant changes of $-PNA_{b_i}$, among which all except one agree on the sign of increase, indicating an intensification of the North Pacific trough. The MEM of $-PNA_{b_i}$ shows an increase of 9.5 m with the 95% confidence interval of 5.9–13.1 m, and the signal-to-noise ratio (i.e., change value is divided by the estimation of unforced internal variability) is 2.3. To a lesser extent, the ridge over western Canada appears to be weakened, since eight models which exhibit significant changes of PNA_{c_i} are agreeable on the sign of decrease except ACCESS1.3. The MEM of PNA_{c_i} shows a decrease of -3.0 m with the 95% confidence interval of -0.7 to -5.3 m, but the signal-to-noise ratio is 0.9. The other two centers, however, do not show significant changes. As a whole, the MEM of PNA_i is increased by 7.5 m with the 95% confidence interval of 0.3–14.7 m, and the signal-to-noise ratio is 1.1. Also, we find that the variance contribution

of the PNA pattern in all models, except CMCC-CM and NorESM1-M, is increased by 4.1–8.8% in the RCP8.5 scenario (Table 3). Overall, the intensity of positive PNA is projected to be strengthened in a warmer climate, which is primarily manifested in the large deepening of the North Pacific trough.

In addition, the North Pacific trough expands northeastward, which can clearly be seen from the difference of spatial pattern between the RCP8.5 and historical runs. Comparing the MEM patterns in Fig. 5a, b, the central area of trough in the twenty-first century, outlined by the isoline of -80 m, expands about two times that in the twentieth century. A difference map (Fig. 5c) clearly shows negative anomalies in the northeastern flank of the North Pacific trough, indicating a northeastward expansion of trough. This feature is robustly manifested in the majority of models. As shown in Fig. 6, other than CMCC-CM, NorESM1-M and CESM1(CAM5), all models show negative anomalies over the Gulf of Alaska and western Canada, which is accompanied by positive anomalies in the downstream. Note that on the basis of the idealized experiments with an atmospheric general circulation model, Zhou et al. (2014) have reported that the ENSO-forced PNA-like teleconnection pattern strengthens and moves eastward under global warming.

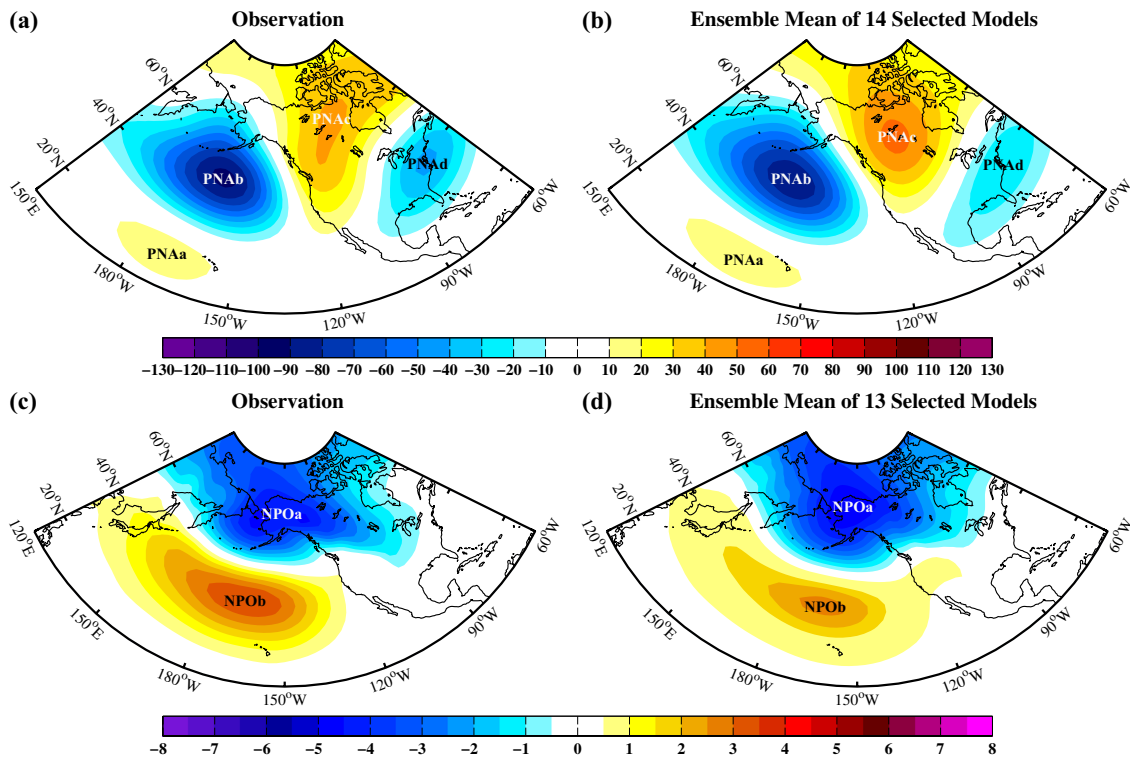


Fig. 3 **a** PNA pattern (m) and **c** NPO pattern (hPa) in winter corresponding to the normalized PC1 of 500-hPa GPHa and PC2 of SLPa. **b, d** As in **a, c**, but for the ensemble-mean of patterns from 14 to 13

selected models, respectively. Percentages of total variance explained by the PNA and NPO in observation are 29.8 and 20.0%, respectively

We speculate that changes in the ENSO-forced PNA-like teleconnection in a warmer climate can also strongly affect future projection of the PNA variability especially on inter-annual time scales.

We further inspect differences in power spectra between the RCP8.5 and historical runs for the monthly EC time series of PNA. Figure 8a suggests that noticeable change primarily occurs on interannual time scales. By scrutinizing the projected changes in the mean power of spectral peaks in the range of 2–8 years which is a typical period of ENSO, it is found that the mean power tends to increase under greenhouse forcing (Fig. 8b). Note that although NorESM1-M shows a decrease of normalized variance at 2–8 years, the periodicity with significant power clearly shifts from 2–4 to 4–8 years, suggesting increased power at lower frequencies. Hence, results may imply that the ENSO-forced teleconnection would have a greater contribution to the PNA change in a warmer climate. Following this lead, we will investigate possible role of tropical Pacific SST in driving the significant response of PNA to greenhouse warming in Sect. 5.

4.2 NPO

Compared with the projected change in the PNA, the response of the NPO to greenhouse warming is much less

robust, with large uncertainty among models. Comparison of the model-averaged NPO patterns in the historical and RCP8.5 runs (Fig. 5d–f) shows a deepening of low pressure over Alaska and a weakening of high pressure in the subtropics. However, there is no consensus on the direction of change in the NPO intensity among models. As shown in Fig. 4b, 9 out of 13 models exhibit significant changes of NPO_i , however, among which five models show an increase while four models show a decrease. This is primarily due to the large diversity of changes in the southern lobe of NPO, as can be seen from four models predicting the significant increase of $NPOb_i$ versus five models predicting the opposite. For the northern lobe of NPO, the intensity tends to be strengthened in the twenty-first century, but only six models show the significant increase of $-NPOa_i$. Furthermore, from Fig. 7, it is clear that changes in the spatial patterns vary largely among models, with a great difference in the changes over the central North Pacific. For example, four models (ACCESS1.0, FGOALS-g2, GISS-E2-R, IPSL-CM5A-MR) show negative anomalies over the central North Pacific, whereas the other four models (CMCC-CESM, HadGEM2-AO, IPSL-CM5A-LR, MPI-ESM-LR) shows the opposite. The projected change in the spectral power of NPO (Fig. 8c, d) also displays a lack of consensus. Table 3 further suggests that the variance contribution of the NPO pattern appears

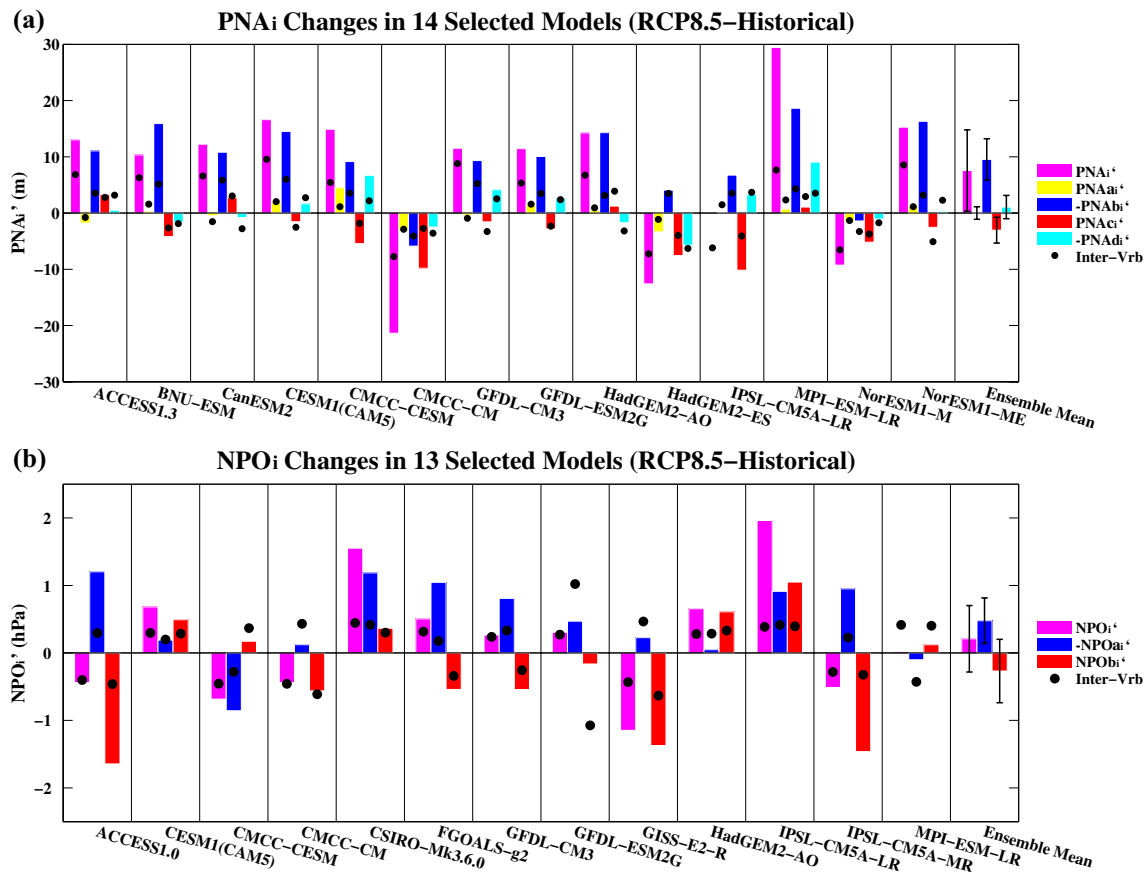


Fig. 4 Changes in the intensities of PNA (m)/NPO (hPa) and its each center of action in positive phase from the historical run to the RCP8.5 run in the selected models. See Sect. 2.2 for details on the definition of intensity of both modes. *Black dot* denotes the estimation of unforced internal variability based on the PI run. *Error bar*

denotes the 95% confidence interval based on a two-tailed student's *t* test. Note that the absolute intensity of each center was used to calculate the projected change so that the *positive (negative)* value indicates the intensification (weakening) of central intensity

to be increased in the RCP8.5 run, but with a much lower magnitude of change than that of the PNA.

5 Role of tropical Pacific Ocean in driving the projected intensification of PNA

5.1 Observational results: extratropical teleconnection driven by anomalous SST in the tropical eastern/central Pacific and its connection with PNA

Many pioneering studies have demonstrated that the tropical Pacific SST anomalies (SSTa), particularly associated with ENSO variability, are one of the principal driving forces of the PNA variability (e.g., Horel and Wallace 1981). Winter-to-winter variability of tropical Pacific SSTa is largely accounted for by ENSO SST variability, which includes two different centers of action, i.e., SSTa centered in the tropical eastern Pacific (EP) and central Pacific (CP) in association with the EP El Niño and CP El Niño (e.g., Kao and

Yu 2009), respectively. Based on the CMIP3 multi-model outputs, Yeh et al. (2009) found that the occurrence ratio of the CP El Niño to the EP El Niño increases under global warming projection, suggesting that more of the CP El Niño events would occur at the expense of the conventional El Niño as global warming intensifies (Ashok and Yamagata 2009). By examining CMIP5 models, Cai et al. (2015) also pointed out that the variability of the tropical CP SSTa is increased in a warmer climate, which has a stronger inter-model consensus than the tropical EP SSTa has. Given that, we may hypothesize that the influence of the tropical CP SSTa on the extratropical atmosphere could exceed that of the tropical EP SSTa in a warmer climate through exciting a stronger fluctuation of the Rossby wave train at midlatitudes.

The EP El Niño and CP El Niño events are suitably described by the area-averaged SSTa in the Niño3 region (5°S–5°N, 150°W–90°W) and Niño4 region (5°S–5°N, 160°E–150°W), respectively, as both regions cover the general traits of ENSO-induced signal. However, the Niño3 and Niño4 indices are highly correlated, which

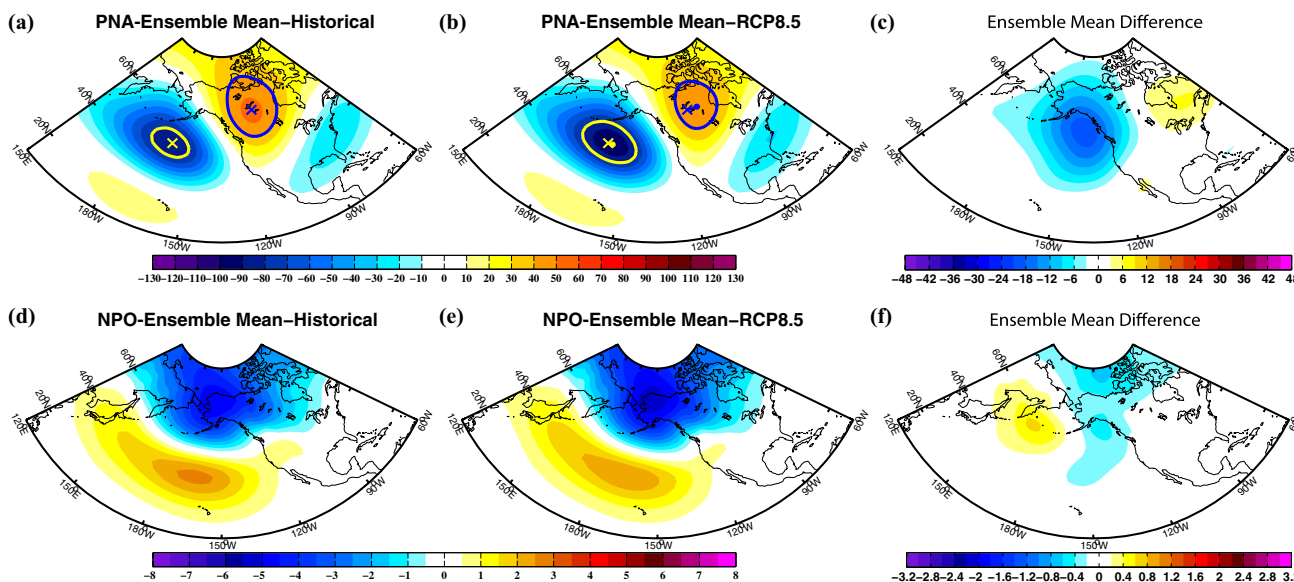


Fig. 5 The MEM of PNA patterns (m) of 14 models in **a** the historical run and **b** the RCP8.5 run and **c** their difference (RCP8.5 minus historical). Only two centers showing significant change (Fig. 4a for reference) are outlined by the isoline of -80 and 40 m for both runs,

and marked by *cross* (*dot*) to signify the position of center in the historical (RCP8.5) run. **d–f** As in **a–c**, but for the MEM of NPO patterns (hPa) of 13 models

contains mixed signals in terms of different ENSO behaviors. Here in order to highlight different centers of action of SSTa in the tropical EP and CP, we employ the EP and CP indices (I_{EP} and I_{CP}) defined by Ren and Jin (2011) as:

$$\begin{cases} I_{EP} = N_3 - \alpha N_4 \\ I_{CP} = N_4 - \alpha N_3 \end{cases} \quad \alpha = \begin{cases} 2/5, & N_3 N_4 > 0 \\ 0, & N_3 N_4 \leq 0 \end{cases}$$

where N_3 and N_4 denote the Niño3 and Niño4 indices, respectively, derived from SSTa in DJF. I_{EP} and I_{CP} are a piecewise linear combination of the Niño3 and Niño4 indices. It is verified that I_{EP} and I_{CP} are nearly uncorrelated ($r=0.23$), whereas N_3 and N_4 are highly correlated ($r=0.81$) in the entire twentieth century. Results also hold for either the first half or the second half of the twentieth century.

Next, we regress the winter SSTa onto the normalized I_{EP} and I_{CP} indices to examine whether the maximum warm anomalies in the tropical EP and CP are well separated from each other. As shown in the first row of Fig. 9, spatial patterns of SSTa capture two well-defined warm centers in the equatorial cold-tongue and warm-pool regions, with the maximum SSTa of 1.1 and 0.7 °C, respectively. In particular, the I_{CP} -derived SSTa pattern is similar to the CP El Niño pattern (Kao and Yu 2009), suggesting that variation of I_{CP} primarily reflects signals of CP ENSO events.

We also examine the surface and mid-tropospheric teleconnections at midlatitudes induced by the tropical EP and CP SSTa, respectively, by regressing the winter SLPa

and 500-hPa GPHa onto the normalized I_{EP} and I_{CP} indices. To the first-order, the extratropical responses to the tropical EP and CP SSTa are similar, which can be seen from anomalous surface low and mid-tropospheric trough over the North Pacific Ocean with a quasi-barotropic structure, as well as anomalous ridge and trough over North America, akin to a PNA-like pattern (see the last two rows of Fig. 9). This is consistent with the result obtained from long model integrations by Garfinkel et al. (2013). Nevertheless, there are subtle spatial differences between the two regression patterns: compared with the response to EP SSTa, the trough/low over the North Pacific Ocean extends further into subtropics and the center of ridge (trough) over North America is further west (east) for the response to CP SSTa. Further comparing such SSTa-forced teleconnections with the PNA pattern shown in Fig. 3a, however, it is suggested that the PNA pattern reflects mixed features of the remote mid-tropospheric responses to the tropical EP and CP SSTa, as pointed out by Weng et al. (2009). As for the SLP response, it should be noted that results do not rule out the finding of Di Lorenzo et al. (2010), which reveals the important influence of CP El Niño on the variability of southern lobe of NPO (i.e., SLPa near Hawaii) especially on decadal time scales.

To further inspect the relationship between the PNA and the teleconnection forced by the tropical EP/CP SSTa, we compare the time evolution of intensities of the PNA variability and the SSTa-forced GPH teleconnection at 500-hPa. The time evolution of the PNA intensity is constructed

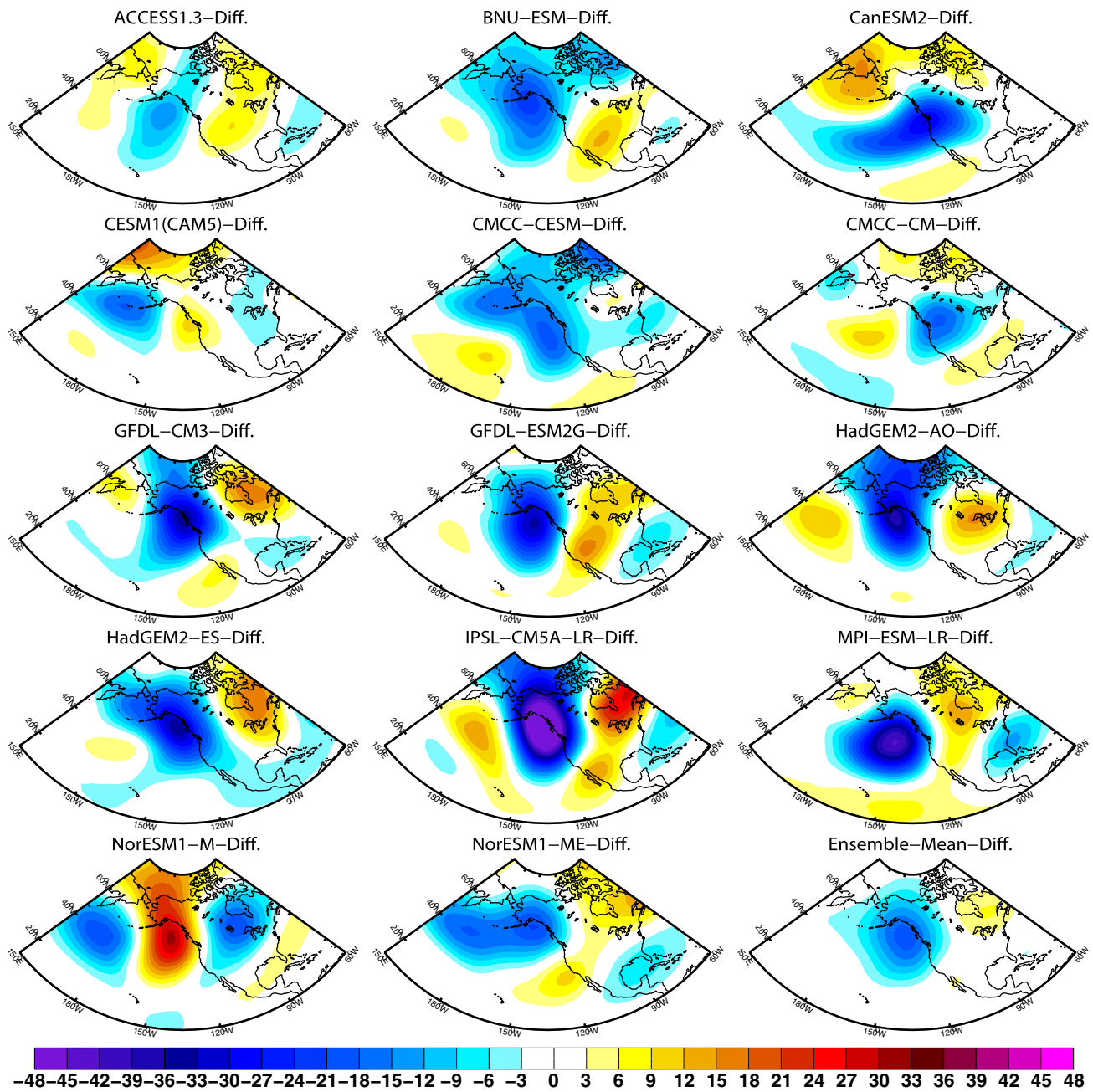


Fig. 6 Difference maps of PNA patterns (m) between the historical and RCP8.5 runs (RCP8.5 minus historical)

over 56 50-year sliding windows (i.e., 1900–1949, 1901–1950, ..., 1955–2004). Here the PNA intensity in each sliding window is derived from the linear combination of four absolute regressions of winter 500-hPa GPHa against the PNA index in the specific 50-year. The four absolute regressions are absolute regression coefficients area-averaged in the four boxes centered on the quadrupole of PNA pattern [PNAa(10°–20°N, 160°–175°W), PNAb(35°–50°N, 140°–160°W), PNAc(55°–70°N, 100°–120°W), PNAd(35°–45°N, 70°–90°W)]. Likewise, the

tropical-SSTa-forced counterparts are calculated based on the area-averaged regressions of 500-hPa GPHa against the normalized I_{EP} and I_{CP} indices in the same boxes. Note that similar results are obtained when using larger boxes. Here the statistical significance of correlation coefficient between the time series based on 50/30-year sliding windows is tested with a two-tailed student’s t test using the effective sample size, which takes into account the serial autocorrelation at lag one (Bretherton et al. 1999). The effective sample size (N_e) is defined as $N_e = N \times (1 - r_x \times r_y) / (1 + r_x \times r_y)$, where

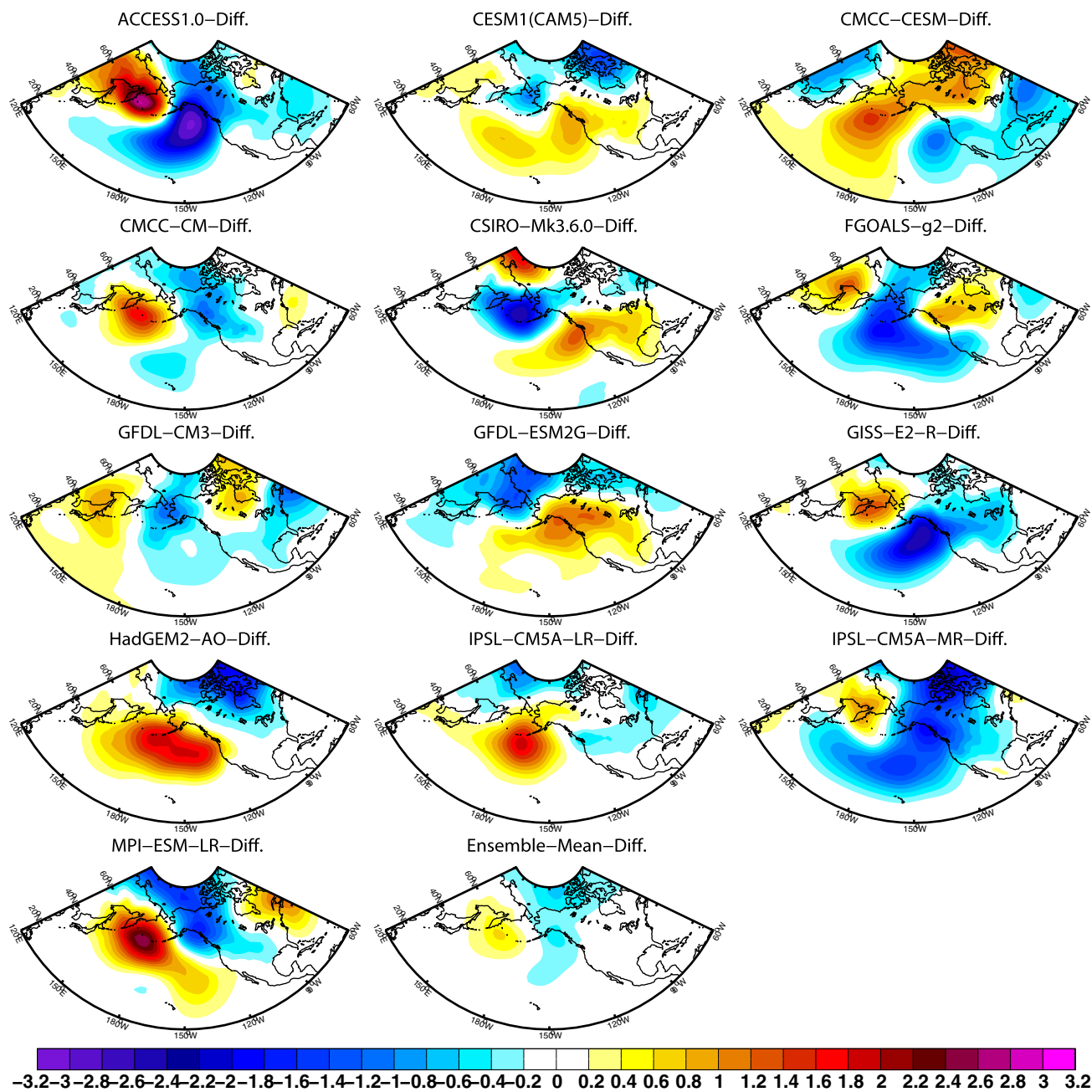


Fig. 7 As in Fig. 6, but for NPO patterns (hPa)

N is the length of time series and $r_x(r_y)$ is the lag-one auto-correlation coefficient of the time series for variable $x(y)$.

As shown in Fig. 10a, the intensity of PNA variability has undergone multidecadal modulation during the twentieth century, which likely reflects strong influence of the natural variability at midlatitudes. This evolution of the PNA intensity is, however, closely related to that of the teleconnection forced by the tropical CP SSTa rather than EP SSTa, with correlation coefficient reaching 0.62 for CP-SSTa forcing versus -0.47 for EP-SSTa forcing. Particularly, we examine

the time evolution of the North Pacific trough (PNA_b) intensity (Fig. 10b, black line), which is found to dominate the PNA intensity evolution (Fig. 10a, black line), given the high correlation coefficient of 0.82. It is also obvious that there is a close association between the multidecadal evolution of the North Pacific trough intensity associated with the PNA variability and that forced by the tropical CP SSTa, with correlation coefficient of 0.68 (Fig. 10b). Indeed, such close relationship can also be found in the time evolution over 76 30-year sliding windows (i.e., 1900–1929, 1901–1930,

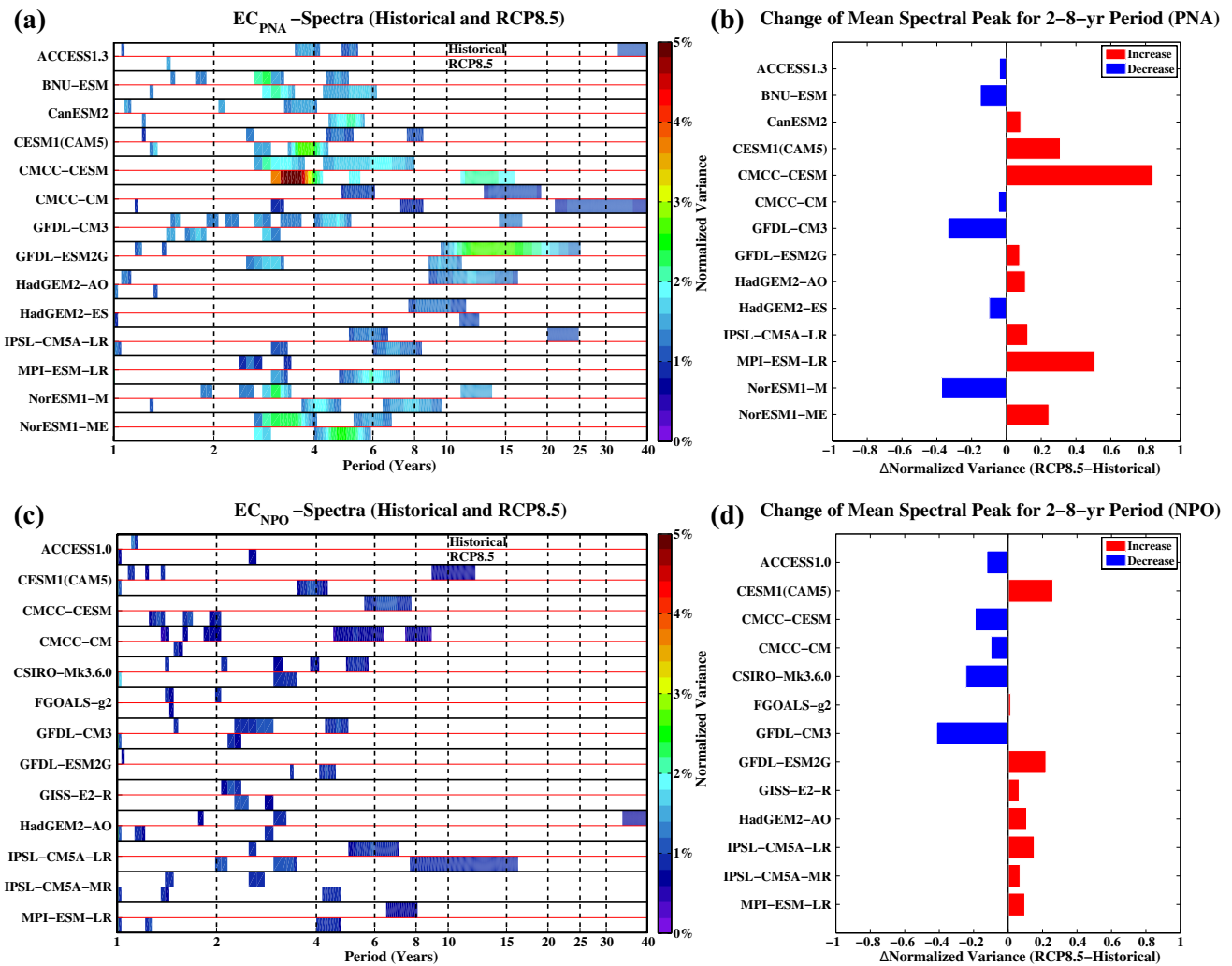


Fig. 8 Power spectra (% of total variance explained) of the monthly EC time series of **a** PNA and **c** NPO for the historical and RCP8.5 runs. Only significant power value (over the 90% confidence level) for each run is shaded and separated by the red line. Projected changes

in the mean spectral power of the monthly EC time series represent for **b** PNA and **d** NPO on interannual time scales, which are derived by taking the differences in the mean power of spectral peaks in the range of 2–8 years between the RCP8.5 and historical runs

..., 1975–2004; Fig. 10c). Therefore, these results suggest an intimate connection of the teleconnection forced by the tropical CP SST variation with the PNA variability in regard to its change with time, which may be expected to also act under climate change scenario.

5.2 Modeling results: role of SST variation in the tropical central Pacific under greenhouse forcing

Given the finding above, we turn to inspect how the extratropical teleconnection forced by the tropical EP/CP SSTa changes in a warmer climate and whether it contributes to the significant projected intensification of the PNA. Note that here we focus on the North Pacific trough, given that its large deepening primarily reflects the intensification of PNA

(recall Sect. 4.1). In this subsection, 11 models which show significant changes in both PNA_i and $-PNAB_i$ (see Fig. 4a for reference) are analyzed. Using a coordinate transformation in the N_3-N_4 phase space (see details in Ren and Jin 2011), we calculate the parameter α in individual models to guarantee that I_{EP} and I_{CP} in each model are uncorrelated. We exclude BNU-ESM because of its unavailability of SST data.

Figure 11 shows the regression patterns of winter SSTa and 500-hPa GPHa against the normalized I_{EP} and I_{CP} indices in the historical simulations. The MEM patterns of SSTa (Fig. 11, upper panels) clearly display two well-defined warm centers in the equatorial cold-tongue and warm-pool regions, with a large resemblance to the observational patterns (Fig. 9). But specifically, the magnitude of simulated warm SSTa center in the cold-tongue region is about 0.2 °C larger than the observation and the

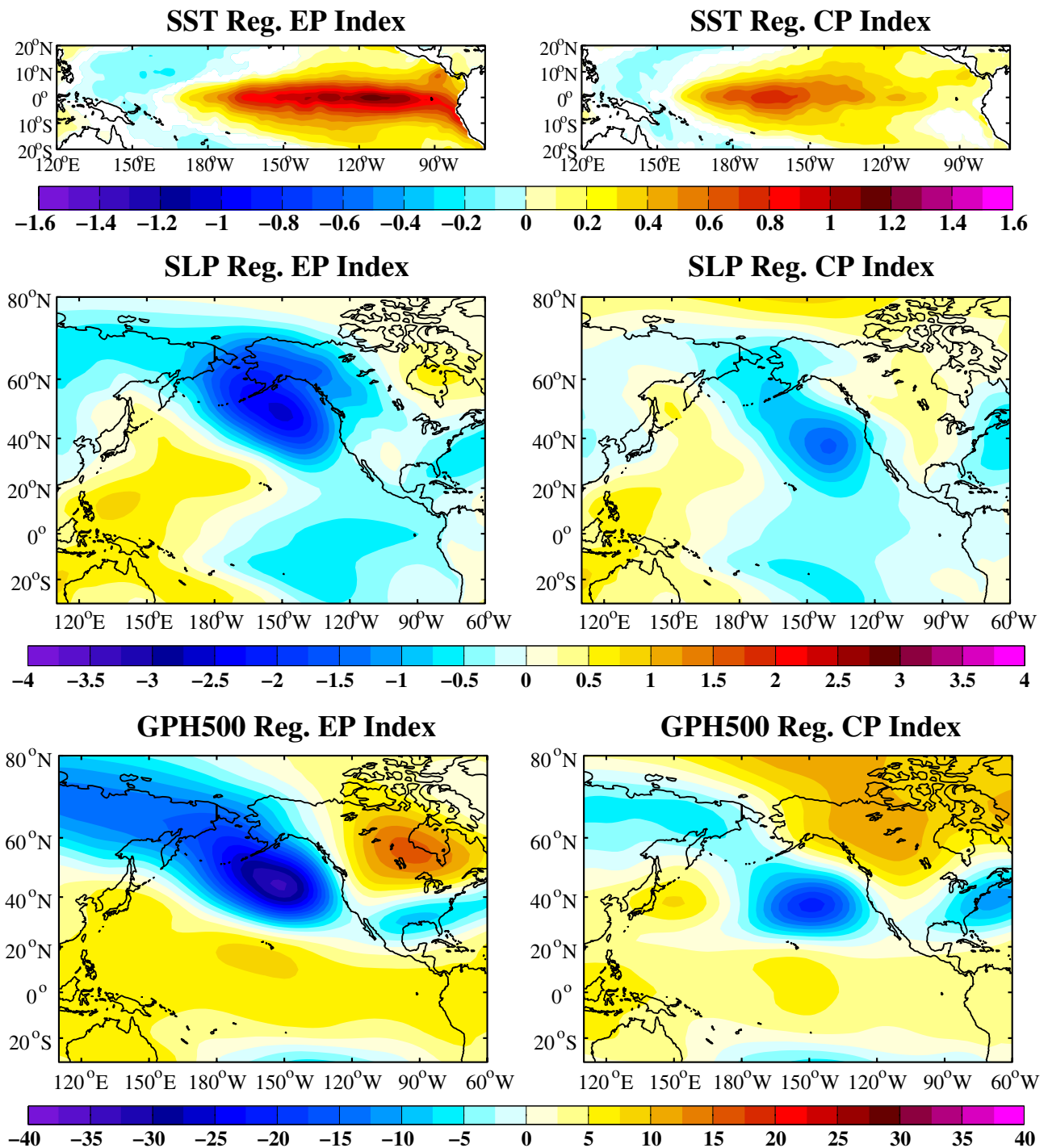


Fig. 9 Winter regression patterns of SSTa (°C), SLPa (hPa) and 500-hPa GPHa (m) onto the normalized (left panels) I_{EP} and (right panels) I_{CP} indices during 1900–2005. Absolute regression coefficients larger than 0.03 °C, 0.1 hPa and 1.3 m are significant at the 95% confidence level

warm SSTa center in the warm-pool region shifts westward by about 10° in the models. Nevertheless, the model simulations generally portray observational features of the extratropical teleconnections forced by the tropical EP and CP SSTa. The MEM patterns of GPHa for EP-SSTa and

CP-SSTa forcing (Fig. 11, middle panels) are correlated with the observational counterparts at 0.79 and 0.76, respectively. Particularly, most models capture the subtle spatial differences between the responses of GPHa to the tropical EP and CP SSTa, such as a slight southward shift

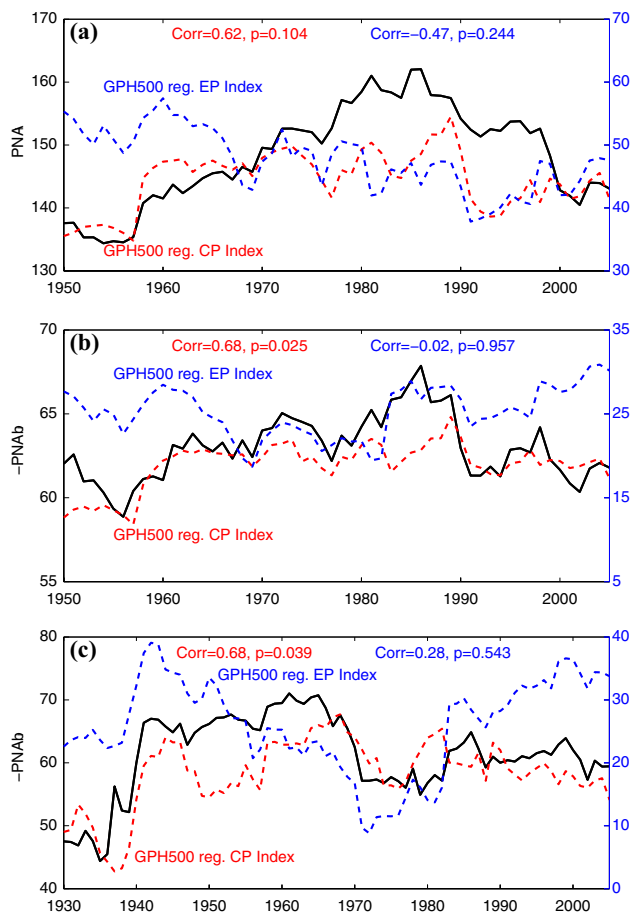


Fig. 10 **a** Time evolution of intensities of the PNA variability (*black line*; *m*) and the tropical-SSTa-forced teleconnection (*red dashed line* for the tropical CP SSTA, *blue* one for the tropical EP SSTA) in winter over 50-year sliding windows starting at every year from 1900 to 2005. **b** As in **a**, but for the North Pacific trough (denoted as PNAb in Fig. 3a) associated with the PNA variability and the tropical-SSTa-forced counterpart. **c** As in **b**, but for 30-year sliding windows. See Sect. 5.1 for details. Correlation coefficient between *black line* and *red (blue)* line is shown in *red (blue)* color, along with the corresponding *p* value. The last year of each sliding window is plotted on the x-axis

of the trough over North Pacific (Fig. 12). In addition, a westward shift of the ridge over North America can also be found for the CP-SSTA-forced teleconnection, albeit with a lower degree of inter-model consensus.

As the climate warms under the RCP8.5 scenario, it is found that the PNA-like teleconnection associated with the tropical CP SST variation is intensified and slightly expands eastward (Fig. 11, lower-right panel). Particularly, the North Pacific trough is deepened by about 9 m (significant at the 95% confidence level based on a two-tailed student's *t* test). However, for the teleconnection induced by the tropical EP SST variation, no significant change in the central intensity

of the North Pacific trough is detected, whereas its spatial shape tends to elongate and tilt northwestward (Fig. 11, lower-left panel). Besides, the trough over southern North America forced by EP-SSTA is largely intensified. Based on these results, we hypothesize that the projected intensification of the CP-SSTA-forced teleconnection is likely to be of great importance in the intensification of PNA in a warmer climate.

To further support this hypothesis, we examine the relationship between the projected changes in the intensity of the North Pacific trough associated with the PNA variability (which dominates the change of PNA intensity) and the counterpart forced by the tropical EP/CP SSTA, by inspecting the time evolution over 171 30-year sliding windows (i.e., 1900–1929, 1901–1930, ..., 2070–2099), following the analysis in Fig. 10. Here the North Pacific domain for the area-average of 500-hPa GPHa in each model (denoted as a dashed box in Fig. 12) covers both centers of the North Pacific troughs forced by the tropical EP and CP SSTA. As shown in Fig. 13, the MEM result clearly illustrates that the long-term evolution of the North Pacific trough associated with the PNA variability is in line with that of the counterpart forced by the tropical CP SSTA rather than EP SSTA. Particularly, from 2006 and onward, the intensities of both North Pacific troughs associated with the PNA variability and CP-SSTA forcing are increased gradually, whereas the tendency of the EP-SSTA-forced trough is downward. As for portrayals of individual models, results show that all models, except CMCC-CM and NorESM1-ME, capture the close relationship between the time evolutions of the North Pacific trough intensity associated with the PNA variability and the counterpart forced by the tropical CP SSTA, given the more significant and higher correlation coefficients for the CP-SSTA forcing than the EP-SSTA forcing. Therefore, the PNA-like teleconnection associated with the SST variation in the tropical CP rather than EP is indeed intensified as climate warms, which contributes to the intensification of PNA variability.

It is well known that the tropical Pacific SSTA can force a planetary Rossby wave train in the extratropical atmosphere through the anomalous upper-level divergence driven by latent heat release in the tropical precipitation (e.g., Hoskins and Karoly 1981; Trenberth et al. 1998; Lu et al. 2004). A natural question arises as to how the anomalous precipitation associated with the tropical CP SST variation changes in a warmer climate and whether its change relates to the deepening of the North Pacific trough associated with the PNA variability. Figure 14 shows the MEM regression patterns of winter tropical SSTA and precipitation against the normalized I_{CP} index in the historical run and their projected changes in the RCP8.5 run. It is obvious that the tropical CP SSTA is increased and expanded eastward under greenhouse

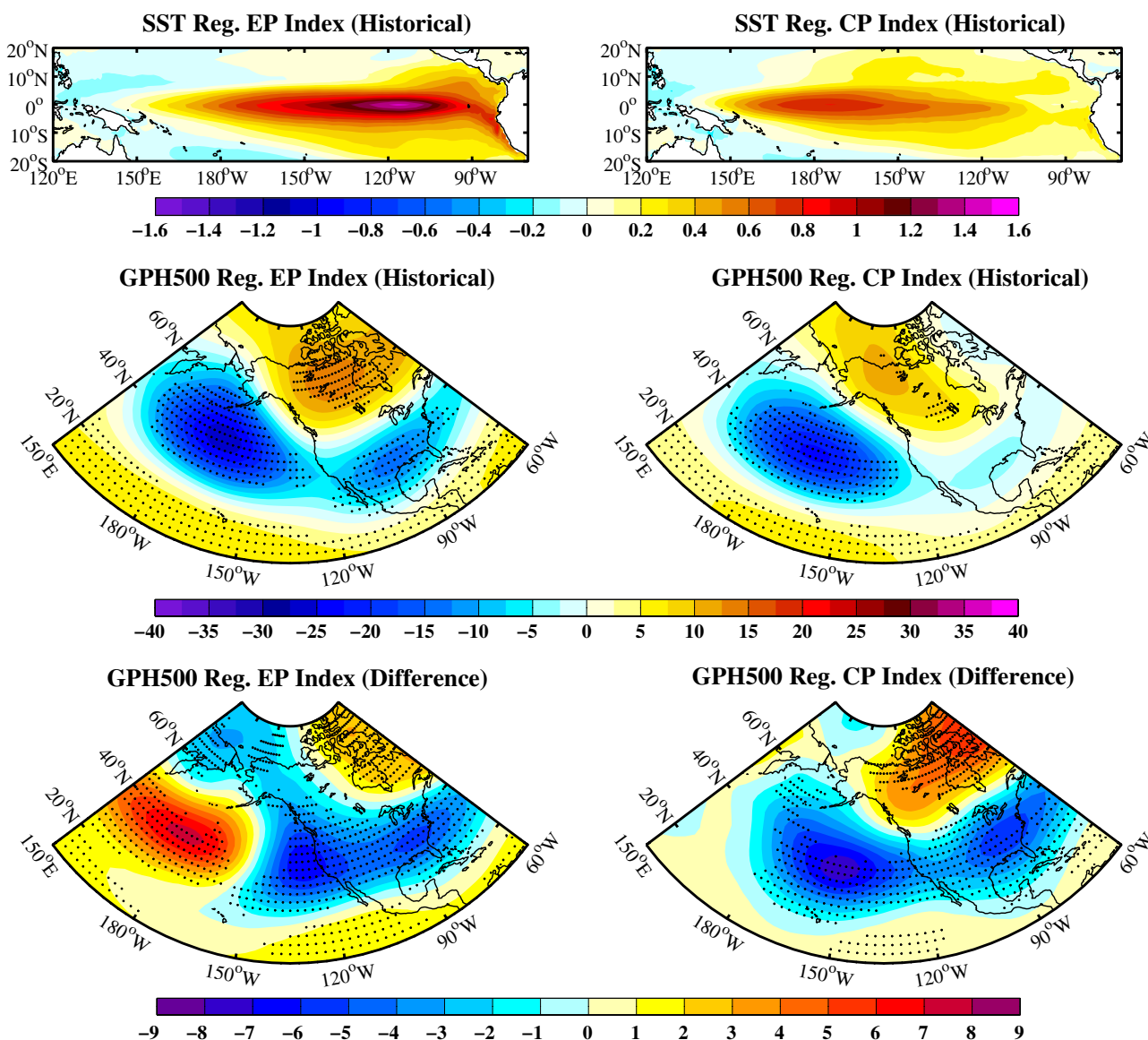


Fig. 11 The MEM of regression patterns of (*upper panels*) winter SSTa (°C) and (*middle panels*) 500-hPa GPHa (m) onto the normalized (*left*) I_{EP} and (*right*) I_{CP} indices derived from the historical runs (1900–2005) of 11 selected models. (*lower panels*) The MEM difference of regression patterns of winter 500-hPa GPHa (m) between the

historical and RCP8.5 runs (RCP8.5 minus historical). *Stippling in middle panels and lower panels* indicate regions where at least 8 of 11 models show regressions significant at the 95% confidence level and agree on the sign of the difference, respectively

forcing, with the largest increase of about 0.2 °C along equatorial band of 180°–150°W. Correspondingly, the maximum center of precipitation anomalies induced by the tropical CP SSTa is significantly intensified by about 42% of that in the past climate, and expands eastward from approximately 160°E to the date line.

Following the analysis in Fig. 13, we further examine the time evolution of the tropical precipitation anomalies induced by the tropical CP SSTa and compare it with that of the North Pacific trough intensity associated with the PNA variability. Here the tropical Pacific domain for the

area-average of precipitation anomalies in each model is set as a box (10° in latitude and 30° in longitude) covering the maximum precipitation responses in both the historical and RCP8.5 runs. From Fig. 15, it can clearly be seen that all models, except CMCC-CM, exhibit a quasi-unidirectional increasing trend of the tropical precipitation response to the CP SSTa over the entire twenty-first century. In addition, the long-term evolution of the tropical precipitation response significantly covaries with that of the North Pacific trough intensity. This is captured by all models (see the correlation coefficients in Fig. 15), except

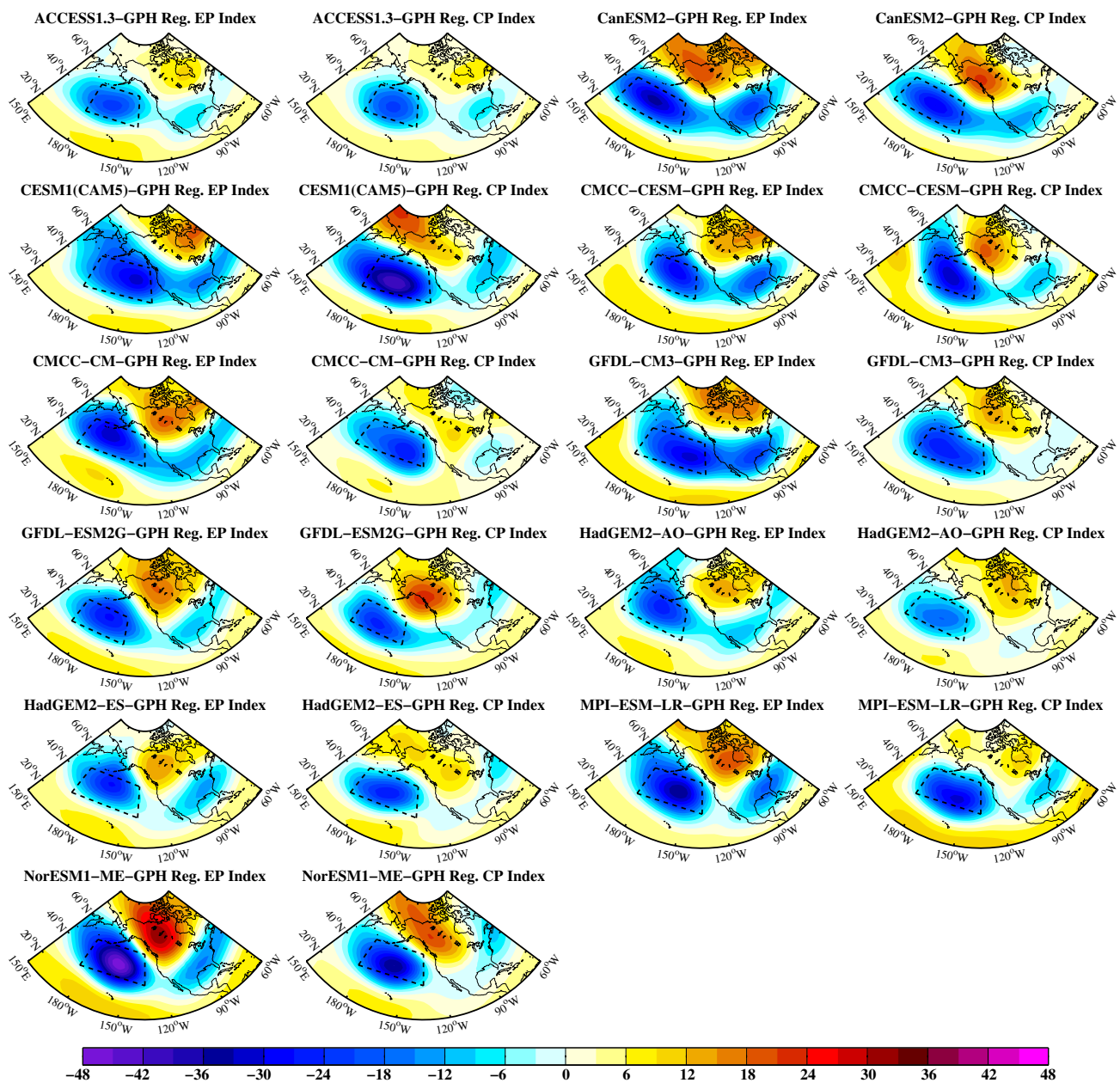


Fig. 12 As in Fig. 11 (middle panels), but for the 11 selected models. Dashed box denotes the domain used for the analysis in Fig. 13

CMCC-CM which shows a downward trend of the North Pacific trough intensity. Therefore, results above suggest that the tropical precipitation response to the CP SST variation is intensified in a warmer climate and in turn facilitates the enhancement of the PNA-like teleconnection (see Fig. 11, lower-right panel), which makes an important contribution to the large deepening of the North Pacific trough associated with the PNA variability.

While the projected deepening of North Pacific trough is robust on the multi-model average, individual model portrayals vary primarily in magnitude (recall $-PNA b_i$ in

Fig. 4a). An issue arises as to what extent inter-model differences in the $-PNA b_i$ projections are related to that in the projections of the tropical Pacific CP/EP SST variability and its associated atmospheric responses. Figure 16 (left panels) show that most models project an intensification of the CP-SSTa-forced trough (with the MEM increased by 6.01 m significant at the 95% confidence level), concurrent with the intensified $-PNA b_i$, whereas the EP-SSTa-forced trough appears to be weakened, with a larger inter-model diversity. In addition, inter-model differences in the projections of trough forced by the tropical CP SSTa rather than

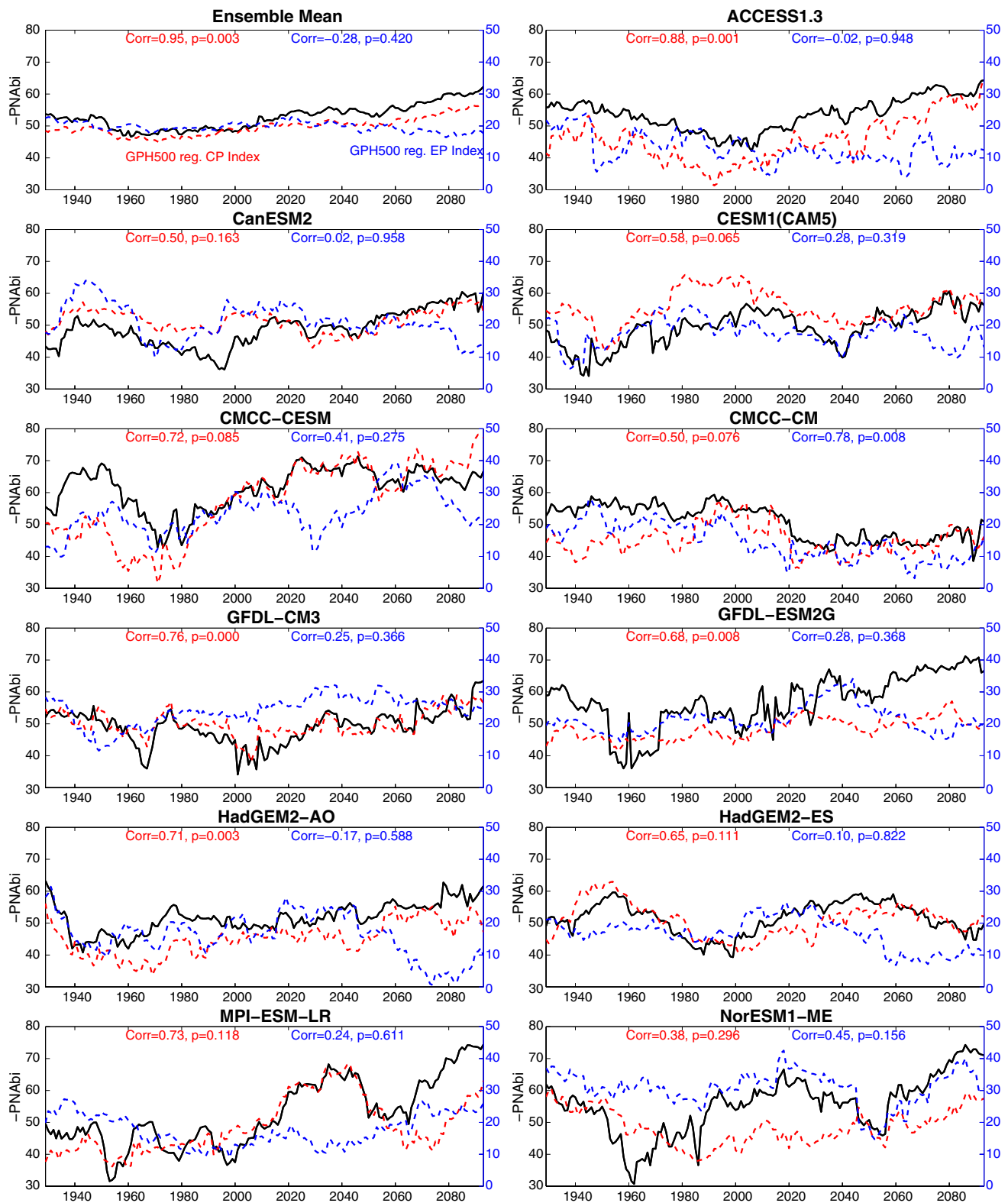


Fig. 13 Time evolution of the North Pacific trough intensity associated with the PNA variability (*black line*; *m*) and the tropical-SSTA-forced counterpart (*red dashed line* for the tropical CP SSTA, *blue* one for the tropical EP SSTA) in winter over 30-year sliding windows

starting at every year from 1900 to 2100 for the MEM and individual models. Correlation coefficient between *black line* and *red (blue) line* is shown in *red (blue) color*, along with the corresponding *p* value. The last year of each sliding window is plotted on the x-axis

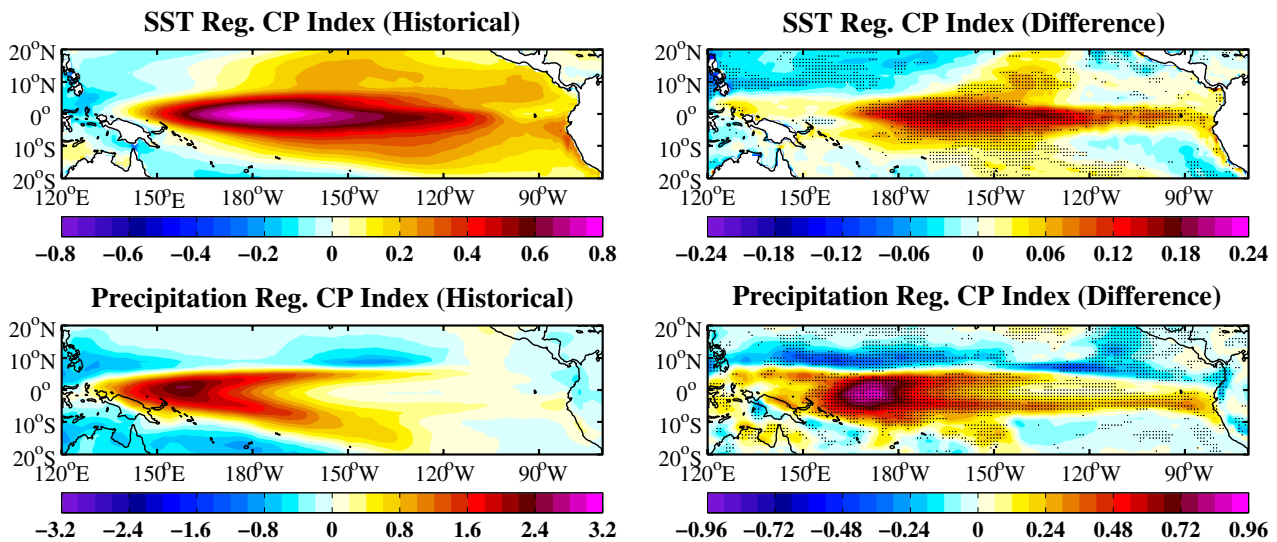


Fig. 14 The MEM of regression patterns of winter SSTa ($^{\circ}\text{C}$) and precipitation anomalies (mm day^{-1}) onto the normalized I_{CP} index in (left panels) the historical run and (right panels) the correspond-

ing changes from the historical run to the RCP8.5 run (RCP8.5 minus historical). Stippling indicates region where at least 8 of 11 models agree on the sign of the difference

EP SSTa largely account for the inter-model diversity of the $-PNA_b_i$ projections, given the high correlation coefficient across models. Such intimate linkage also holds for the tropical precipitation anomalies forced by the CP SSTa (i.e., anomalous tropical diabatic heating), given the correlation coefficient reaching 0.83 across models when excluding the outlier CMCC-CM (Fig. 16, middle panels). It is noticeable that the MEM of precipitation response to the CP SSTa is increased by 0.66 mm day^{-1} (about 37% of that in the twentieth century), which is in fact significant above the 99% confidence level. The inter-model consensus is strong, with none of the models producing a reduction. In stark contrast, the tropical precipitation response to the EP SSTa possesses a large uncertainty. Taking an in-depth look into the projected changes in the amplitudes of tropical CP and EP SST variabilities [i.e., standard deviations of the I_{EP} and I_{CP} indices; $\sigma(I_{CP})$, $\sigma(I_{EP})$], we also find a close inter-model relationship between the projections of $\sigma(I_{CP})$ and $-PNA_b_i$ (Fig. 16, right panels), with the significant correlation coefficient of 0.79 excluding the outlier. However, it should be noted that the projected increase of $\sigma(I_{CP})$ shows a weaker robustness than does the tropical precipitation response to the CP SSTa. Overall, results above suggest that, on average, models with stronger intensification of the tropical CP SST variability and its associated precipitation response tend to have larger deepening magnitude of the North Pacific trough associated with the PNA variability. Results also further confirm the important role of the intensification of the tropical precipitation anomalies induced by the CP SSTa rather than the EP SSTa in driving the deepened North Pacific trough in a warmer climate.

6 Summary and discussion

We evaluate the representation of spatiotemporal features of PNA and NPO in the historical simulations from 30 to 32 CMIP5 models, respectively, by comparing with the observed counterparts during the twentieth century winter-time. The majority (80%) of models reasonably simulate either the geographical distribution or the amplitude of PNA/NPO pattern. However, only half of models can reliably reproduce both features in space. Particularly, compared with the PNA simulations, the ability to simulate the NPO is worse and more dispersed among models. As for the temporal features, variabilities of the PNA and NPO in majority of models are biased toward higher amplitude. We also find that the percentage of total variance in heights explained by the PNA variability is underestimated by most CMIP5 models (21/30), which is contrary to the simulations of CMIP3 models (Stoner et al. 2009). The spectral analysis further shows that, in observation, the PNA variability has significant interannual- and decadal-scale spectrum, with two peaks in the range of 1–2 and 4–6 years and highest power in the 20–25 years, whereas the NPO variability exhibits only a significant peak at 2–4 years. Most models can simulate the interannual variabilities of PNA and NPO, qualitatively consistent with the observation, albeit with the significant spectral peaks varying in the range of 1–6 years. However, models generally lack the ability to reproduce the decadal (20–25 years) variability of PNA.

We further select 14 and 13 models to investigate the 21st-century changes in the intensities of PNA and NPO forced by greenhouse warming, respectively. These selected

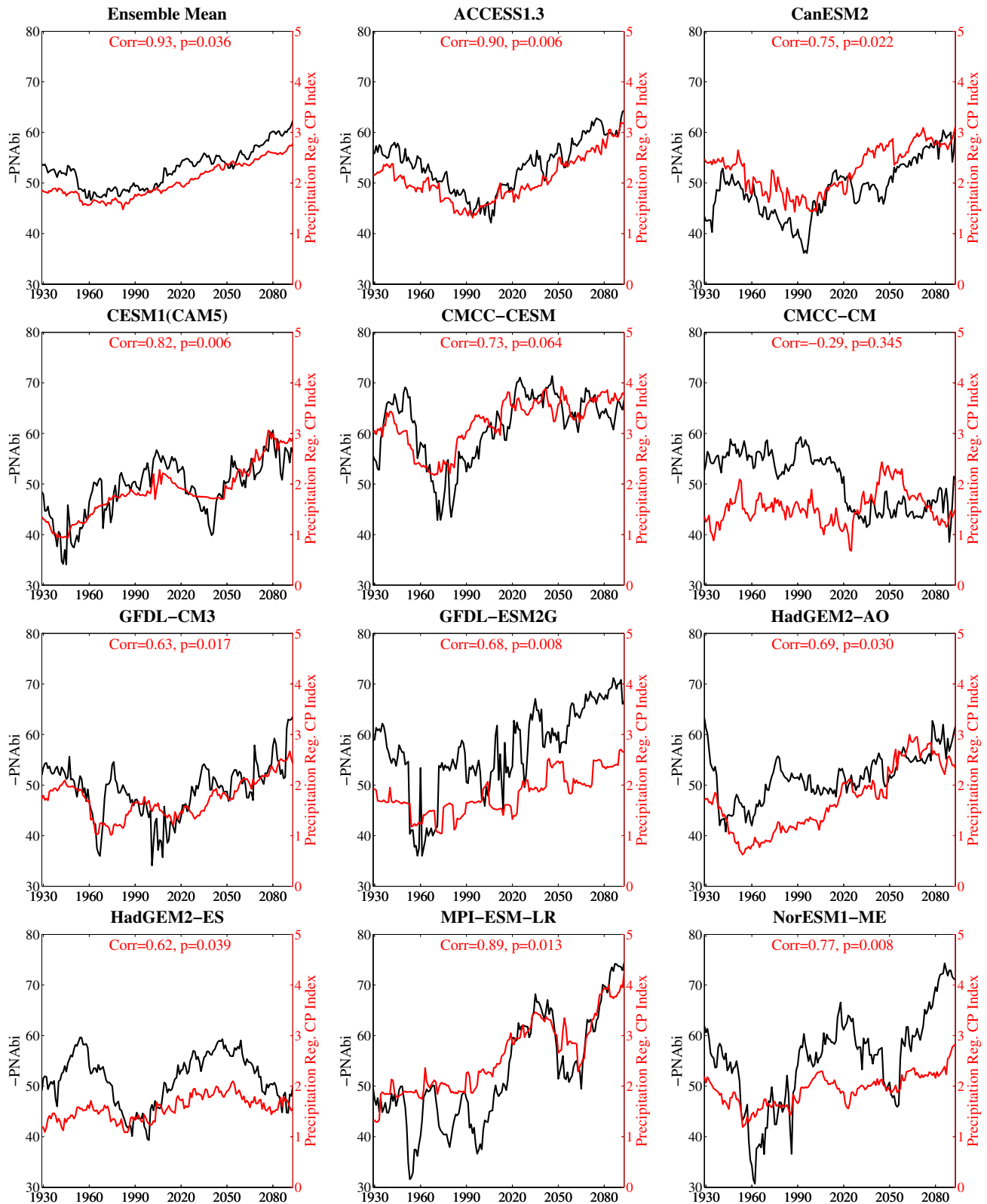


Fig. 15 Time evolution of the North Pacific trough intensity associated with the PNA variability (*black line*; m; same as in Fig. 13) and the tropical CP-SSTa-forced precipitation anomalies (*red line*; mm day⁻¹) in winter over 30-year sliding windows starting at every year

from 1900 to 2100 for the MEM and individual models. Correlation coefficient between two lines and the corresponding *p* value are given in each subplot. The last year of each sliding window is plotted on the x-axis

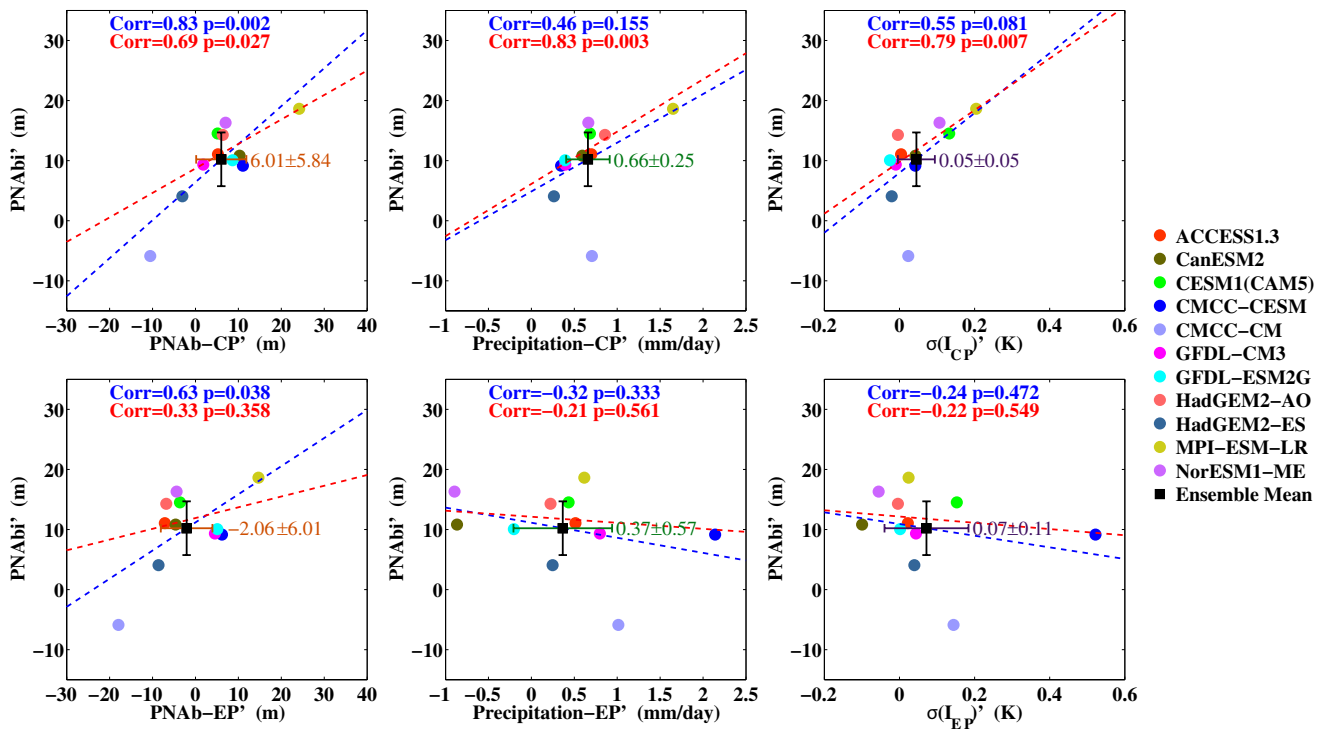


Fig. 16 Scatter diagram of the projected changes in the North Pacific trough intensity ($-PNAb_i$; same as blue bar in Fig. 4a) versus changes in (left panels) the trough intensity and (middle panels) precipitation anomalies driven by the tropical (upper) CP SSTA and (lower) EP SSTA as well as (right panels) the amplitudes of tropical CP and EP SSTA variabilities [$\sigma(I_{CP})$, $\sigma(I_{EP})$] across models. Changes are derived from the 95-year-interval difference between the historical and RCP8.5 runs (RCP8.5 minus historical). The corresponding multi-

model means and their uncertainties based on a two-tailed student's *t* test at the 95% confidence level are indicated by a square with error bars, with nearby values showing for the three variables mentioned in the x-axis. The projected change in the $-PNAb_i$ is 10.22 ± 4.47 m. Lines denote the linear regression including (blue) and excluding (red) the outlier CMCC-CM that projects a weakening of the $-PNAb_i$, with the corresponding correlation coefficients and *p* values shown in blue (red) color

models well represent the observed structure and amplitude of PNA and NPO in space, especially for the North Pacific trough and the anomalous low pressure over Alaska. It is found that the PNA intensity is projected to be strengthened in a warmer climate, whereas there is no consensus on the direction of change in the NPO intensity among models. The intensification of positive PNA is primarily manifested in the large deepening of the North Pacific trough and its north-eastward expansion. Specifically, the North Pacific trough deepens about 9.5 ± 3.6 m (the 95% confidence interval) in the twenty-first century, which is 2.3 times the unforced internal variability, and the central area of trough (outlined by the isoline of -80 m) expands about two times that in the twentieth century. In addition, we find that the spectral power of PNA on interannual time scales (2–8 years) tends to be increased under greenhouse forcing, implying that the ENSO-forced teleconnection could be in the position of more influence in a warmer climate. Following this lead, we investigate possible role of tropical Pacific Ocean in driving the significant response of PNA to greenhouse warming.

In observation and model simulations, results show that the PNA pattern reflects mixed features of the PNA-like

wave trains in responding to the tropical EP and CP SSTA, which is consistent with the previous studies (e.g., Hoerling and Kumar 2002; Weng et al. 2009; Garfinkel et al. 2013). In regard to time evolution during the twentieth century, however, it is found that the multidecadal evolutions of the North Pacific trough intensity, which dominates the PNA intensity evolution, is closely related to that of the counterpart in the PNA-like teleconnection forced by the tropical CP SSTA rather than EP SSTA. As the climate warms in the twenty-first century, the PNA-like teleconnection forced by the tropical CP SSTA rather than EP SSTA is found to be intensified, in part owing to the robust enhancement of the tropical precipitation response to the CP SST variation, which makes an important contribution to the intensification of PNA variability. Indeed, models with stronger intensification of the tropical CP SST variability and its associated precipitation response tend to have larger deepening magnitude of the North Pacific trough associated with the PNA variability. However, we do not find the significant relationship between inter-model differences in the projections of North Pacific trough intensity associated with the PNA variability and that of tropical EP

SST variability and its associated atmospheric responses. Here, it should be noted that the projected increase of the amplitude of tropical CP SST variability shows a weaker robustness than does the tropical precipitation response to the CP SSTa, albeit that the MEM increase of the former (0.05 °C) is about 1.5 times the unforced internal variability. Overall, our results may suggest that in a warmer climate the tropical and extratropical atmosphere is more sensitive to the perturbation of SST in the tropical CP region rather than EP region, even though how the tropical CP or EP SST variability responds to greenhouse warming remains uncertain.

Along with the tropical diabatic heating, the anomalous transient eddy vorticity flux divergence at midlatitudes plays an important role in regulating the PNA-like response of extratropical atmospheric circulation (e.g., Held et al. 1989; Hoerling and Ting 1994; Jin et al. 2006). Jin et al. (2006) pointed out that the tropically-forced Rossby wave train tends to perturb synoptic-scale eddy activity in an organized manner to further enhance the extratropical teleconnection. Thus, in addition to the intensified tropical heating, one would expect feedback between synoptic eddy and low-frequency flow at midlatitudes to facilitate the intensification of the PNA-like teleconnection in a warmer climate. To what extent such eddy-mediated process is relevant for the response of PNA to greenhouse warming is left for future study.

In the present study, although the intensification of the PNA-like teleconnection forced by the tropical CP SSTa can explain the increased intensity of the North Pacific trough (blue bar in Fig. 4a), a northeastward expansion of trough which is manifested as the negative GPHa difference over the Gulf of Alaska (see Fig. 5c) may be resulted from other processes. One possible process involves changes in the tropospheric time-mean flow at mid- and high-latitudes, which is suggested to be able to modulate stationary waves (Branstator 1984; Kang 1990; Meehl and Teng 2007). We examine the projected changes in the mean state of zonal wind at 500 hPa in winter and its relationship with the negative GPHa differences over the Gulf of Alaska. The preliminary result suggests that a strengthening of mean easterly flow over the Chukchi Peninsula appears to facilitate a northeastward expansion of the North Pacific trough (not shown), which needs to be further verified.

Acknowledgements We acknowledge the WCRP's Working Group on Coupled Modelling, which is responsible for CMIP, and we thank the climate modeling groups for producing and making available their model output. This work was supported by National Key Research and Development Program of China (2016YFA0601804), China National Global Change Major Research Project (2013CB956201), National Natural Science Foundation of China (NSFC) Projects (41506009, 41490643, 41130859, 41490640, 41506016, 41521091).

Open Access This article is distributed under the terms of the Creative Commons Attribution 4.0 International License (<http://creativecommons.org/licenses/by/4.0/>), which permits unrestricted use, distribution, and reproduction in any medium, provided you give appropriate credit to the original author(s) and the source, provide a link to the Creative Commons license, and indicate if changes were made.

References

- Alexander MA, Blade I, Newman M, Lanzante JR, Lau NC, Scott JD (2002) The atmospheric bridge: the influence of ENSO teleconnections on air-sea interaction over the global oceans. *J Clim* 15:2205–2231
- Allan AM, Hostetler SW, Alder JR (2014) Analysis of the present and future winter Pacific-North American teleconnection in the ECHAM5 global and RegCM3 regional climate models. *Clim Dyn* 42:1671–1682
- Ashok K, Yamagata T (2009) The El Niño with a difference. *Nature* 461:481–484
- Barnston AG, Livezey RE (1987) Classification, seasonality and persistence of low frequency atmospheric circulation patterns. *Mon Weather Rev* 115:1825–1850
- Branstator G (1984) The relationship between zonal mean flow and quasi-stationary waves in the midtroposphere. *J Atmos Sci* 41:2163–2178
- Bretherton CS, Widmann M, Dymnikov VP, Wallace JM, Bladé I (1999) The effective number of spatial degrees of freedom of a time-varying field. *J Clim* 12:1990–2009
- Cai W, Santoso A, Wang G et al (2015) ENSO and greenhouse warming. *Nat Clim Change* 5:849–859
- Chhak KC et al (2009) Forcing of low-frequency ocean variability in the northeast Pacific. *J Clim* 22:1255–1276
- Christensen JH et al (2013) Climate phenomena and their relevance for future regional climate change. In: *Climate change 2013: the physical science basis. Contribution of Working Group I to the Fifth Assessment Report of the Intergovernmental Panel on Climate Change*. Cambridge University Press, Cambridge
- Compo GP, Whitaker JS, Sardeshmukh PD, Matsui N, Allan BJ, Yin X, Gleason BE, Vose RS, Rutledge G et al (2011) The twentieth century reanalysis project. *Q J R Meteorol Soc* 137:1–28. doi:10.1002/qj.776
- Croci-Maspoli M, Schwierz C, Davies HC (2007) Atmospheric blocking: space-time links to the NAO and PNA. *Clim Dyn* 29:713–725
- Deser C, Phillips AS, Hurrell JW (2004) Pacific interdecadal climate variability: linkages between the tropics and the North Pacific during boreal winter since 1900. *J Clim* 17:3109–3124
- Di Lorenzo E, Schneider N, Cobb KM, Franks PJS, Chhak K, Miller AJ, McWilliams JC, Bograd SJ, Arango H, Curchitser E, Powell TM (2008) North Pacific Gyre Oscillation links ocean climate and ecosystem change. *Geophys Res Lett* 35:L08607. doi:10.1029/2007GL032838
- Di Lorenzo E, Cobb KM, Furtado JC, Schneider N, Anderson BT, Bracco A, Alexander MA, Vimont DJ (2010) Central Pacific El Niño and decadal climate change in the North Pacific Ocean. *Nat Geosci* 3:762–765. doi:10.1038/NNGEO984
- Furtado JC, Lorenzo ED, Schneider N, Bond NA (2011) North Pacific decadal variability and climate change in the IPCC AR4 models. *J Clim* 24:3049–3067
- Garfinkel CI, Hurwitz MM, Waugh DW, Butler AH (2013) Are the teleconnections of Central Pacific and Eastern Pacific El Niño distinct in boreal wintertime? *Clim Dyn* 41:1–18

- Ge Y, Gong G (2009) North American snow depth and climate teleconnection patterns. *J Clim* 22:217–233
- Harding KJ, Snyder PK (2015) The relationship between the Pacific-North American teleconnection pattern, the great plains low-level jet, and North Central US heavy rainfall events. *J Clim* 28:6729–6742
- Held IM, Lyons SW, Nigam S (1989) Transients and the extratropical response to El Niño. *J Atmos Sci* 46:163–174
- Hoerling MP, Kumar A (2002) Atmospheric response patterns associated with tropical forcing. *J Clim* 15:2184–2203
- Hoerling M, Ting M (1994) Organization of extratropical transients during El Niño. *J Clim* 7:745–766
- Horel JD, Wallace JM (1981) Planetary-scale atmospheric phenomena associated with the Southern Oscillation. *Mon Weather Rev* 109:813–829
- Hoskins B, Karoly D (1981) The steady linear response of a spherical atmosphere to thermal and orographic forcing. *J Atmos Sci* 38:1179–1196
- Jin F-F, Pan LL, Watanabe M (2006) Dynamics of synoptic eddy and low-frequency flow interaction. Part I: a linear closure. *J Atmos Sci* 63:1677–1694
- Kang IS (1990) Influence of zonal mean flow change on stationary wave fluctuations. *J Atmos Sci* 47:141–147
- Kao HY, Yu JY (2009) Contrasting Eastern-Pacific and Central-Pacific types of ENSO. *J Clim* 22:615–632
- Latif M, Barnett TP (1996) Decadal climate variability over the North Pacific and North America: dynamics and predictability. *J Clim* 9:2407–2423
- Lau N-C (1988) Variability of the observed midlatitude storm tracks in relation to low-frequency changes in the circulation pattern. *J Atmos Sci* 45:2718–2743
- Leathers DJ, Yarnal B, Palecki MA (1991) The Pacific/North American teleconnection pattern and United States climate. Part I: regional temperature and precipitation associations. *J Clim* 4:517–528
- Linkin ME, Nigam S (2008) The North Pacific Oscillation-West Pacific teleconnection pattern: mature-phase structure and winter impacts. *J Clim* 21:1979–1997
- Lu J, Greatbatch RJ, Peterson KA (2004) Trend in Northern hemisphere winter atmospheric circulation during the last half of the twentieth century. *J Clim* 17:3745–3760
- Meehl GA, Teng H (2007) Multi-model changes in El Niño teleconnections over North America in a future warmer climate. *Clim Dyn* 29:779–790
- Nigam S (2003) Teleconnections. In: Holton JR, Pyle JA, Curry JA (eds) *Encyclopedia of atmospheric sciences*. Academic, London, pp 2243–2269
- Poli P, Hersbach H, Dee DP et al (2016) ERA-20C: an atmospheric reanalysis of the 20th century. *J Clim* 29:4083–4097
- Rayner NA, Parker DE, Horton EB, Folland CK, Alexander LV, Rowell D, Kent EC, Kaplan A (2003) Global analyses of sea surface temperature, sea ice, and night marine air temperature since the late nineteenth century. *J Geophys Res* 108:4407. doi:10.1029/2002JD002670
- Ren H-L, Jin F-F (2011) Niño indices for two types of ENSO. *Geophys Res Lett* 38:L04704. doi:10.1029/2010GL046031
- Rogers JC (1990) Patterns of low-frequency monthly sea-level pressure variability (1899–1986) and associated wave cyclone frequencies. *J Clim* 3:1364–1379
- Stoner K, Hayhoe K, Wuebbles DJ (2009) Assessing general circulation model simulations of atmospheric teleconnection patterns. *J Clim* 22(16):4348–4372
- Taylor KE (2001) Summarizing multiple aspects of model performance in a single diagram. *J Geophys Res* 106:7183–7192
- Taylor KE, Stouffer RJ, Meehl GA (2012) An overview of CMIP5 and the experiment design. *Bull Am Meteorol Soc* 93(4):485–498. doi:10.1175/BAMS-D-11-00094.1
- Torrence C, Compo GP (1998) A practical guide to wavelet analysis. *Bull Am Meteorol Soc* 79:61–78
- Trenberth KE, Branstator GW, Karoly D, Kumar A, Lau NC, Ropelewski C (1998) Progress during TOGA in understanding and modeling global teleconnections associated with tropical sea surface temperatures. *J Geophys Res* 103:14291–14324
- Wallace JM, Gutzler DS (1981) Teleconnections in the geopotential height field during the northern hemisphere winter. *Mon Weather Rev* 109:784–812
- Weng H, Behera S, Yamagata T (2009) Anomalous winter climate conditions in the Pacific Rim during recent El Niño Modoki and El Niño events. *Clim Dyn* 32:663–674. doi:10.1007/s00382-008-0394-6
- Wettstein JJ, Wallace JM (2010) Observed patterns of month-to-month storm track variability and their relationship to the background flow. *J Atmos Sci* 67:1420–1437
- Yeh S-W, Kug J-S, Dewitte B, Kwon M-H, Kirtman BP, Jin FF (2009) El Niño in a changing climate. *Nature* 461:511–514
- Yu JY, Kim ST (2011) Relationships between Extratropical Sea level pressure variations and the Central Pacific and Eastern Pacific types of ENSO. *J Clim* 24:708–720
- Zhou Z-Q, Xie S-P, Zheng X-T, Liu Q, Wang H (2014) Global warming-induced change in El Niño teleconnections over the north Pacific and North America. *J Clim* 27:9050–9064